

# Tracking the Lithiation State of $\text{Li}_x\text{Si}$ from Machine-Learned XPS Binding Energies

Michael Alejandro Hernandez Bertran,<sup>†,‡</sup> Davide Tisi,<sup>¶</sup> Federico Grasselli,<sup>†,‡</sup>

Michele Ceriotti,<sup>¶</sup> Elisa Molinari,<sup>†,‡</sup> and Deborah Prezzi<sup>\*,‡</sup>

<sup>†</sup>*Dipartimento di Scienze Fisiche, Informatiche, Matematiche (FIM), Università di  
Modena e Reggio Emilia, 41125 Modena, Italy*

<sup>‡</sup>*Nanoscience Institute, National Research Council (CNR-NANO), 41125 Modena, Italy*

<sup>¶</sup>*Laboratory of Computational Science and Modeling, Institut des Matériaux, École  
Polytechnique Fédérale de Lausanne, 1015 Lausanne, Switzerland*

E-mail: [deborah.prezzi@cnr.it](mailto:deborah.prezzi@cnr.it)

## Abstract

X-ray Photoelectron Spectroscopy (XPS) is a powerful technique to probe chemical states and interfacial processes in battery materials, but a quantitative interpretation is often hindered by the complex, heterogeneous microstructures that form during operation and dominate electrochemical cycling. Silicon based anodes represent a paradigmatic example in Li batteries, as (de)lithiation proceeds through the formation of strongly disordered  $\text{Li}_x\text{Si}$  phases and crystal-amorphous transformations that are hard to characterize. Here, we introduce a computational framework that combines machine-learning (ML) prediction of core-level binding energies to large-scale atomistic simulations – Grand Canonical Monte Carlo (GCMC) complemented with molecular dynamics (MD), driven by a ML potential – for a systematic sampling of lithiation states and local atomic environments. This approach yields stoichiometry maps that

match the characteristic experimental trends observed in *operando* and *ex situ* XPS measurements, including the distinctive Si 2*p* spectroscopic signatures associated with the crystal-to-amorphous disordering driving early delithiation.

## Introduction

Core-level spectroscopies are established tools/methods to assess the electronic structure and chemical environment of materials. Among these techniques, X-ray Photoelectron Spectroscopy (XPS) stands out as one of the most widespread, allowing both qualitative and quantitative analysis with information depths from a few to tens of nm depending on the radiation source.<sup>1,2</sup> In battery research, XPS is routinely employed to characterize electrode surfaces, providing insights into the oxidation state of redox-active species and the composition of the solid electrolyte interphase (SEI).<sup>3</sup> Recent advances in electrochemical cell design<sup>4,5</sup> and the development of solid electrolytes<sup>6</sup> have enabled XPS measurements *in situ*<sup>7,8</sup> and *operando*,<sup>9-11</sup> which can complement standard *ex-situ* studies<sup>12-14</sup> by capturing interfacial and redox processes under realistic electrochemical conditions. During cycling, however, the probed materials can become highly heterogeneous and structurally complex, sampling disordered and metastable states for which quantitative spectral references are limited, making it difficult to translate measured binding-energy shifts into composition- and structure-resolved information. Extrinsic effects, such as evolving SEI contributions, local electrostatic potentials and differential charging, can further complicate energy referencing and peak assignment.<sup>15</sup>

Silicon-based anodes for Li-ion batteries represent a technologically relevant, stringent test case for XPS quantitative analysis. In fact, Si offers an exceptionally high theoretical capacity (4200 mAh g<sup>-1</sup>), yet its practical use is limited by extreme volume changes and complex phase transformations during cycling, which generate large mechanical stresses and drive particle fracture, pulverization and loss of electrical contact.<sup>16-19</sup> These effects originate from intrinsically nonuniform (de)lithiation within individual particles,<sup>20,21</sup> where Li

concentration gradients induce sharp phase boundaries and anisotropic stresses, especially near interfaces between crystalline  $\text{Li}_{3.75}\text{Si}$  (c- $\text{Li}_{3.75}\text{Si}$ ) and amorphous  $\text{Li}_x\text{Si}$  phases.<sup>22–24</sup> Capturing these processes often demands *operando* techniques with both surface sensitivity and chemical-state resolution.

Complementary *in situ* X-ray diffraction (XRD),<sup>25–27</sup> transmission electron microscopy (TEM),<sup>28–30</sup> and nuclear magnetic resonance (NMR)<sup>31–33</sup> have provided key insights into the structural evolution of Si anodes. XPS adds an element- and chemical-state-resolved specificity, making it well suited to track near-surface lithiation-induced chemical changes. However, its quantitative interpretation has been hindered by the lack of a connection between XPS spectral features and Li concentration in disordered, nonstoichiometric phases that dominate Li–Si (de)lithiation. In this context, recent *operando* XPS measurements on a-Si thin films have established systematic correlations between the Si 2*p* binding energy (BE) and Li content during electrochemical cycling, and identified pronounced spectral shifts as fingerprints of the the formation of c- $\text{Li}_{3.75}\text{Si}$  upon deep lithiation and its amorphization during delithiation.<sup>11</sup> Turning these empirical correlations into quantitative, transferable stoichiometry–spectrum relationships nonetheless remains challenging.

Ab initio approaches based on density functional theory (DFT) can provide core-level BEs and XPS spectra with high accuracy, and are routinely used to support identification of experimental spectral features.<sup>34,35</sup> However, these simulations would become prohibitively expensive for the structurally complex or disordered materials typical of battery applications,<sup>36–40</sup> considering both the large supercells required to model the systems and the statistics required to sample the broad distribution of local environments, each of which needs to be treated separately (i.e., one calculation for each non-equivalent atomic environment). This type of limitations has motivated the impressive rise of machine-learning (ML) strategies, which can approximate DFT-level predictions at far lower cost.<sup>41–43</sup> These methods can be used both to generate realistic atomistic ensembles through ML interatomic potentials (MLIP),<sup>43–57</sup> which support molecular dynamics (MD) simulations of large systems

over extended timescales,<sup>58–72</sup> and to predict target properties directly from local structural descriptors.<sup>73–77</sup>

Here, we combine an uncertainty-aware ML surrogate model for predicting Li 1s and Si 2p core-level BEs with large-scale MD simulations for appropriately sampling Li<sub>x</sub>Si structures across a wide range of compositions. The surrogate model is trained on DFT reference calculations and provides calibrated uncertainty estimates, enabling robust predictions for both crystalline and disordered systems. To generate physically relevant configurations, we employ MD and grand-canonical Monte Carlo (GCMC) simulations driven by a neuro-evolution potential (NEP).<sup>56</sup> Using the resulting ensembles, we construct stoichiometry maps that directly relate XPS peak positions to Li content and structural evolution during delithiation. The resulting trends are consistent with available *operando* and *ex situ* experiments and reveal clear spectroscopic signatures of the crystalline-to-amorphous transition in Li-Si, offering a quantitative interpretation of XPS data from Si-based electrodes under realistic operating conditions.

## Methods

### Core-level binding energies from DFT

The core-level binding energies (BE) were computed using a pseudopotential-based total-energy difference method,<sup>78</sup> using Quantum ESPRESSO<sup>79–81</sup> as DFT engine. Within the excited core-hole (XCH)<sup>82</sup> approximation, the BE of a core state  $n$  for a target atom  $a$  is computed as the difference between the total energy of the excited state  $E^*$ , with an electron removed from the core and placed in valence, and the ground state total energy  $E^0$ :

$$\text{BE}_{a,n} = E^*(\eta_{c,n} - 1, \eta_v + 1) - E^0(\eta_{c,n}, \eta_v) + \Delta E_{\text{corr}}, \quad (1)$$

where  $\eta_{c,n}$  and  $\eta_v$  are the populations of the core state  $n$  and valence, respectively. The correction term  $\Delta E_{\text{corr}}$  contains the relaxation effects of core electrons in the presence of a core-hole<sup>83</sup> for a given exchange-correlation functional<sup>84</sup> as embedded in the core-hole pseudopotential, making the computed BE comparable to experiments. For core states with non-zero orbital angular momentum ( $l \neq 0$ ), the spin-orbit coupling (SOC) contribution was incorporated through the following empirical correction

$$\text{BE}_{a,n,l,j} = \text{BE}_{a,n} + (-1)^{j-l+\frac{3}{2}} \frac{|\Delta_{\text{SOC}}^l|}{2l+1} \left[ j(j+1) - l(l+1) - \frac{3}{4} \right], \quad (2)$$

where  $j$  is one of the two angular momentum values for a given  $l$ , and  $|\Delta_{\text{SOC}}^l|$  is the absolute experimental energy split between them.

The final XPS spectrum for a species  $\mathcal{A}$  and a core-level state  $n$  was computed from the corresponding atomic contributions  $\text{BE}_{a,n}$  as:

$$S_{\mathcal{A},n}(E, \sigma, \Gamma) = \sum_{a \in \mathcal{A}} V(E - \text{BE}_{a,n}, \sigma, \Gamma), \quad (3)$$

where  $a$  runs over all atoms of species  $\mathcal{A}$ , and  $V(\cdot)$  is the empirical line broadening function centered at  $\text{BE}_{a,n}$  and represented by the convolution of the Gaussian and Lorentzian distributions, known as the Voigt profile.<sup>85</sup> The Gaussian broadening  $\sigma$  and the Lorentzian broadening  $\Gamma$  account for the experimental resolution and the lifetime of the core-hole, respectively.

DFT calculations were performed using ultrasoft pseudopotentials with the PBE exchange correlation functional. Core-hole pseudopotentials were generated to describe excited atoms for the simulation of Li 1s and Si 2p BEs, whereas pseudopotentials from the SSSP library v1.1<sup>86</sup> were used to describe ground state atoms. The energy cut-offs for the kinetic energy of the wave functions and the charge density were set to 100 Ry and 800 Ry, respectively. A supercell approach was employed to minimize interactions between excited atoms and their periodic images, maintaining a minimum distance of 8 Å between replicas. The

Brillouin zone corresponding to the supercell was sampled using a Monkhorst-Pack  $k$ -point mesh with a grid spacing of  $0.25 \text{ \AA}^{-1}$ .

## Machine learning model and uncertainty estimation

The BE of a target atom was predicted using kernel ridge regression (KRR),<sup>87</sup> taking its local atomic environment as input, as follows:

$$\hat{y}_* = \sum_{i=1}^N \alpha_i k(\mathbf{X}_*, \mathbf{X}_i) = \sum_{i=1}^N \alpha_i \exp\{-\gamma \|\mathbf{X}_* - \mathbf{X}_i\|^2\}, \quad (4)$$

where  $\hat{y}_*$  is the BE prediction,  $\mathbf{X}_*$  and  $\mathbf{X}_i$  are equivariant feature vectors, representing the local atomic environment of the target atom and the training samples, respectively.  $k(\cdot, \cdot)$  denotes the kernel function, which computes the distance between feature vectors and, in this work, corresponds to an isotropic Gaussian kernel with a length scale parameter  $\ell = 1/\sqrt{2\gamma}$ .

The coefficients  $\alpha_i$  are the dual variables computed as:

$$\boldsymbol{\alpha} = (\mathbf{K} + \lambda \mathbf{I})^{-1} \mathbf{y}, \quad (5)$$

where  $\mathbf{K} = k(\mathbf{X}_i, \mathbf{X}_j)$  is the kernel matrix,  $\lambda > 0$  is the regularization strength, penalizing large values of the regression weights, and  $\mathbf{y}$  is the vector of the training target BEs.

In order to endow the ML predictions with an associated uncertainty, we have constructed a committee of  $M$  equivalent models  $\hat{y}_*^{(m)}$ , by subsampling the training set.<sup>88</sup> Within this framework, it is straightforward to propagate the uncertainty to quantities derived from the original predictions.<sup>89</sup> The ensemble average for a quantity with functional dependence on the predictions,  $\hat{z}_* = f(\hat{y}_*)$ , is defined as

$$\hat{z}_* = \frac{1}{M} \sum_{m=1}^M \hat{z}_*^{(m)}, \quad (6)$$

with the following sample standard deviation

$$s_z(\mathbf{X}_*) = \left( \frac{1}{M-1} \sum_{m=1}^M |\hat{z}_*^{(m)} - \hat{z}_*|^2 \right)^{1/2}, \quad (7)$$

where  $\hat{z}_*^{(m)} = f(\hat{y}_*^{(m)})$  were evaluated across the ensemble. To account for finite-ensemble effects, the standard deviation was calibrated as  $s_z^{(\text{calib.})}(\mathbf{X}_*) = \kappa_z s_z(\mathbf{X}_*)$ , using a scaling factor  $\kappa_z$ , defined for small  $M$  as<sup>89,90</sup>

$$\kappa_z^2 = -\frac{1}{M} + \frac{M-3}{M-1} \frac{1}{N_{\text{val}}} \sum_{i=1}^{N_{\text{val}}} \frac{|z_i - \hat{z}_i|^2}{s_z^2(\mathbf{X}_i)}, \quad (8)$$

where  $z_i$  denotes the reference value (ground-truth) evaluated on the validation dataset  $\{\mathbf{X}_i\}_{i=1}^{N_{\text{val}}}$ .

## Local Atomic Environment Descriptor

Local atomic environments were described using the smooth overlap of atomic positions (SOAP) power spectrum,<sup>91</sup> as implemented in librascal.<sup>92</sup> The atom-centered density was expanded using the Gaussian-type orbital (GTO) basis with  $n_{\text{max}} = 8$  and spherical harmonics with  $l_{\text{max}} = 6$  for the radial and angular parts, respectively. A maximum cut-off radius of 8 Å was applied, such that only atoms within this distance were included in the expansion. Their contributions were smoothly weighted using radial scaling, defined by the function  $f_{\text{cut}}(r) = [1 + (r/r_0)^4]^{-1}$ , with characteristic distance  $r_0$ . The SOAP similarity between two atomic environments  $\mathbf{X}_i$  and  $\mathbf{X}_j$  was measured using the SOAP kernel  $(\mathbf{X}_i \cdot \mathbf{X}_j)^\zeta$ , with  $\zeta = 4$ .

## Dataset and Farthest Point Sampling

We took advantage of an available dataset containing  $\sim 62000$  structures of  $\text{Li}_x\text{Si}$ ,<sup>93</sup> which was originally developed to train a deep potential (DP)<sup>45,94</sup> model for Li-Si battery anodes. The dataset includes ground-state crystalline Li, Si, and  $\text{Li}_x\text{Si}$  phases ( $0 < x < 4.5$ ) from

the Materials Project,<sup>95</sup> expanded through DFT optimization at the PBE level and *ab initio* MD sampling, as well as amorphous a-Li<sub>x</sub>Si configurations generated via iterative DeePMD and grand canonical Monte Carlo approaches, as detailed in Ref. 93.

From the original dataset, two disjoint subsets were constructed for training and validation. For the training set, data sub-selection was performed to ensure uniform sampling across the structures while reducing the computational effort related to DFT-based BE calculations. This was done by sorting the dataset in descending order of structural diversity using Farthest Point Sampling<sup>96</sup> (FPS). The algorithm was initialized with the first structure in the dataset, and in subsequent iterations, it selected the next sample based on the maximum distance criterion, as

$$\langle \mathbf{X} \rangle_k = \operatorname{argmax}_{\langle \mathbf{X} \rangle_k \notin \mathcal{S}} \left( \min_{\langle \mathbf{X} \rangle_j \in \mathcal{S}} \|\langle \mathbf{X} \rangle_k - \langle \mathbf{X} \rangle_j\|^2 \right), \quad (9)$$

where  $\mathcal{S}$  denotes the set of structures selected in the previous steps, and  $\langle \mathbf{X} \rangle_k$  is the  $k$ -th structure-averaged SOAP vector, constructed using  $r_0 = 6 \text{ \AA}$  and an atomic density smoothing  $\sigma_a = 0.3 \text{ \AA}$  for the GTO radial basis. The size of the training set was chosen to ensure that the mean absolute error (MAE) of the model remained below the typical experimental uncertainty for the BE resolution in XPS, i.e., 0.1 eV.<sup>97</sup>

## MD and GCMC Computational Details

The melt-quench-anneal (MQA) protocol employed to generate near-equilibrium amorphous Li<sub>x</sub>Si structures involves an initial melting phase from 2500 K and to 1800 K over 200 ps, followed by three quenching stages: (i) from 1500 K to 1250 K at a rate of  $10^{13} \text{ Ks}^{-1}$ , (ii) from 1250 K to 1050 K at a rate of  $10^{11} \text{ Ks}^{-1}$ , and (iii) from 1050 K to 500 K at a rate of  $10^{13} \text{ Ks}^{-1}$ . The melting and quenching phases were simulated using the isobaric-isothermal (*NPT*) ensemble, at  $P = 0 \text{ bar}$ , by coupling the system (assumed here isotropic) with the stochastic cell rescaling (SCR) barostat<sup>98</sup> and the stochastic velocity rescaling (SVR)

thermostat.<sup>99</sup> After quenching, the atomic positions were further relaxed using the steepest descent method to achieve mechanical equilibrium with a force tolerance of  $10^{-6}$  eVÅ<sup>-1</sup>. The corresponding simulations were performed with GPUMD<sup>56</sup> using a Li-Si neuroevolution potential<sup>56</sup> (NEP) from Ref. 100.

To investigate the early stages of the delithiation process, grand canonical Monte Carlo (GCMC) simulations<sup>101</sup> were carried out starting from different crystalline phases of Li silicides having different initial Li concentration. For each structure, two particle exchanges and one displacement attempt were performed every 50 steps of molecular dynamics (MD) in the *NPT* ensemble, with  $P = 0$  bar and  $T = 300$  K. The chemical potential ( $\mu$ ) was dynamically changed to favor the delithiation process with an acceptance ratio of 44%. The simulations were conducted using LAMMPS<sup>102</sup> compiled with the PWMLFF package for the NEP-LAMMPS interface. MD simulations were performed using a hybrid / overlay setup that combines NEP and Ziegler-Biersack-Littmark<sup>103</sup> (ZBL) potentials to avoid nonphysical bond lengths during volume contraction in the delithiation process.

## Results and discussion

### Model Training and Validation

The general scheme of the training and validation process is depicted in Figure 1, where the individual steps are described in the Methods Section. Starting from the full dataset of Li<sub>x</sub>Si structures, the final training dataset obtained by FPS includes 245 structures, comprising  $\sim 7800$  Li and  $\sim 7800$  Si atomic environments. The validation set – randomly selected from the remaining structures – contains instead 55 structures, with  $\sim 1900$  Li and  $\sim 1900$  Si atomic environments.

For each selected structure in both the training and validation sets, the DFT BEs for Li 1s and Si 2p were computed by exploiting the XpsWorkChain of the aiida-qe-xspec plugin,<sup>104</sup> an automated Python workflow based on AiiDA QUANTUM ESPRESSO<sup>105,106</sup> that imple-

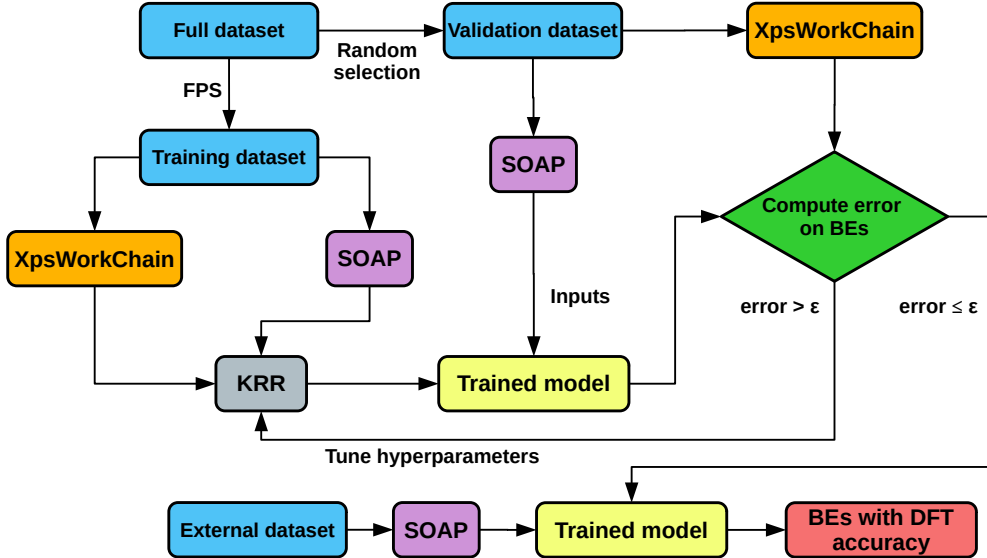


Figure 1: Schematic of the machine-learning workflow for BE prediction, including data generation, training, and validation steps.

ments the calculation XPS BEs as described in the Methods Section. The `XpsWorkChain` has been interfaced seamlessly with our Python workflow for the training and validation of the KRR models, enabling consistency and high-throughput generation of the training data as well as full data provenance as provided by AiiDA. The training of the KRR models was performed with the scikit-learn Python library,<sup>107</sup> using a grid search over the hyperparameters space  $(\lambda, \gamma)$  to find the optimal values that minimize the MAE in a five-fold cross-validation configuration. A total of 12 models were trained for each of the two core-levels, covering all combinations of characteristic distances  $r_0 = 2.5, 3.5, 4.5, 5.5 \text{ \AA}$  and atomic density smoothing values  $\sigma_a = 0.3, 0.4, 0.5 \text{ \AA}$  used for the SOAP descriptors (see Figure S1, Supporting Information). The models with the best bias-variance trade-off, defined here as those that maximize the coefficient of determination  $R^2$  on the validation set while minimizing the difference between the training and validation  $R^2$ , were selected as the optimal models.

Figure 2 presents the training results for the optimal models predicting the Li 1s and Si 2p BEs in the  $\text{Li}_x\text{Si}$  dataset. In the left panels, we present the correlation plots for the Li 1s (a) and Si 2p (c) BEs between the best model predictions and the *ab initio* DFT reference for both the training and the validation set. These models achieved  $R^2$  values of 0.97 and

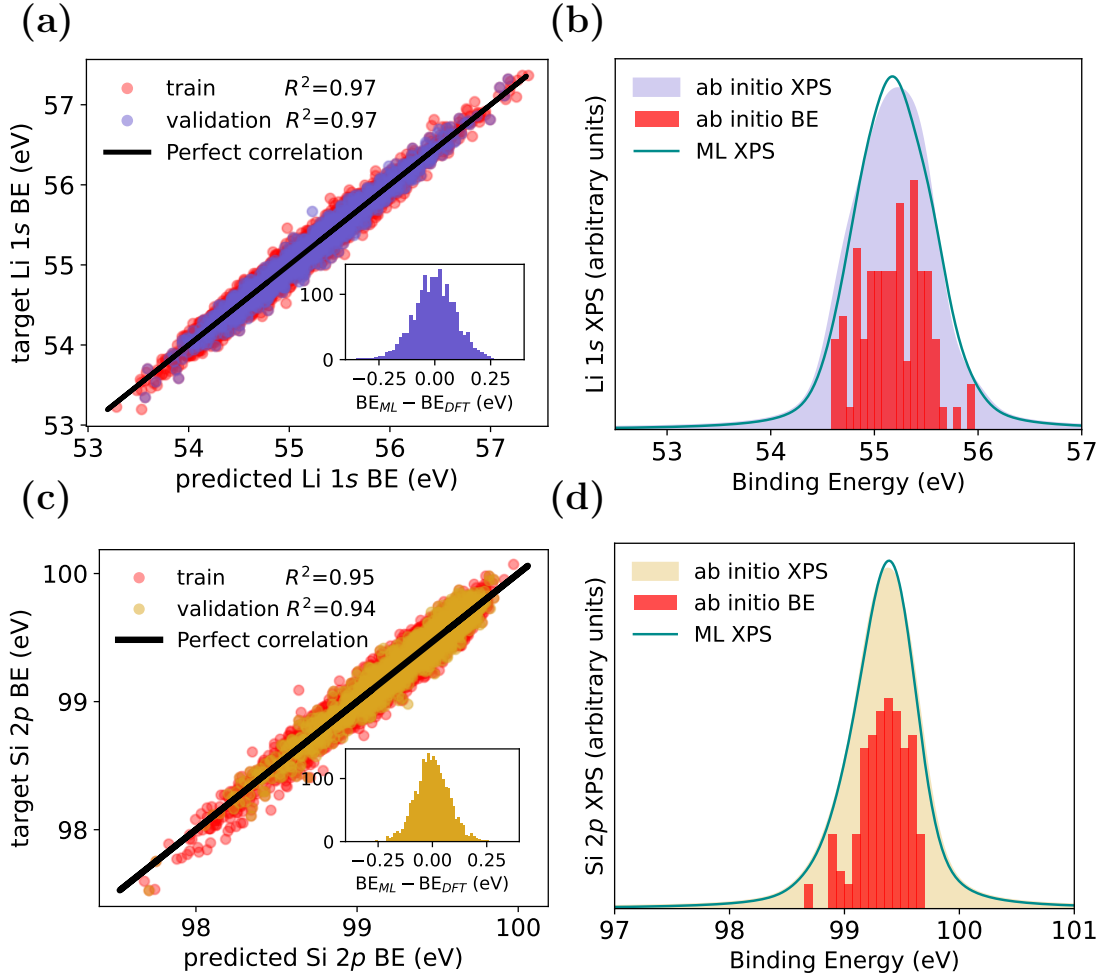


Figure 2: (Left) Performance of the Gaussian KRR models corresponding to the Li 1s (a) and Si 2p (c) for the  $\text{Li}_x\text{Si}$  train and validation sets. The determination coefficient  $R^2$  for the relation between ML predictions and *ab initio* DFT (target) is reported in the legend. The histogram for the difference between BEs obtained with ML and *ab initio* DFT is shown as an inset. (Right) Model benchmarking against DFT XPS obtained for an out-of-sample  $\text{Li}_x\text{Si}$  structure from Ref. 108, the red histograms account for the DFT BEs of Li 1s (b) and Si 2p (d). The colored areas (curves in darkcyan) represent the XPS spectra obtained by adding Voigt profiles centered on the DFT (ML predicted) BEs.

0.94 for Li 1s and Si 2p, respectively. The corresponding hyperparameters, along with the MAE and root mean square error (RMSE) of the best models, are reported in Supporting Information (see Table S1). In order to test their generalization capability, the models were benchmarked against DFT XPS data for an out-of-sample  $\text{Li}_x\text{Si}$  structure from Ref. 108. The chosen structure contains 224 atoms, i.e., well beyond the average and maximum size of the training set (64 and 152 atoms, respectively). The results of the benchmark are reported on the right panels of Figure 2, where the red histograms represent the DFT BEs for the Li 1s (b) and Si 2p (d) core-levels, while the shaded areas and the dark cyan curves correspond to the XPS spectra reconstructed as the sum of Voigt profiles centered on the BEs obtained by DFT and the ML models, respectively. The agreement between the predicted spectra and the reference DFT data demonstrates the transferability of the models beyond the training set.

Uncertainty estimates for the BEs and for  $\text{BE}_{\max} = \underset{E}{\operatorname{argmax}} [S_{\mathcal{A},n}(E, \sigma, \Gamma)]$ , derived from the model predictions, are shown in Figure 3. Overall, the calibrated uncertainties predicted for the BEs (a,c) are consistent with typical XPS experimental resolutions, on average falling below 0.1 eV. For  $\text{BE}_{\max}$  (b,d), the quantity typically monitored in operando experiments, the propagated uncertainty is even smaller, further confirming the reliability of the model predictions.

## Comparison with Experimental Data

The experimental reference data in this work are drawn from two XPS studies on a-Si thin films as model electrodes for Li-ion batteries. In the first study, a-Si thin films deposited on Cu were cycled in a liquid-electrolyte cell, and *ex situ* XPS coupled with scanning electron microscopy (SEM) was used to track the potential-dependent evolution of both the Si electrode and SEI.<sup>109</sup> In the second study, a-Si films were sputter-deposited onto a solid electrolyte  $\text{Li}_{6.6}\text{La}_3\text{Zr}_{1.6}\text{Ta}_{0.4}\text{O}_{12}$  and subjected to electrochemical lithiation and delithiation, which were monitored by *operando* XPS. Upon deep lithiation and subsequent delithiation,

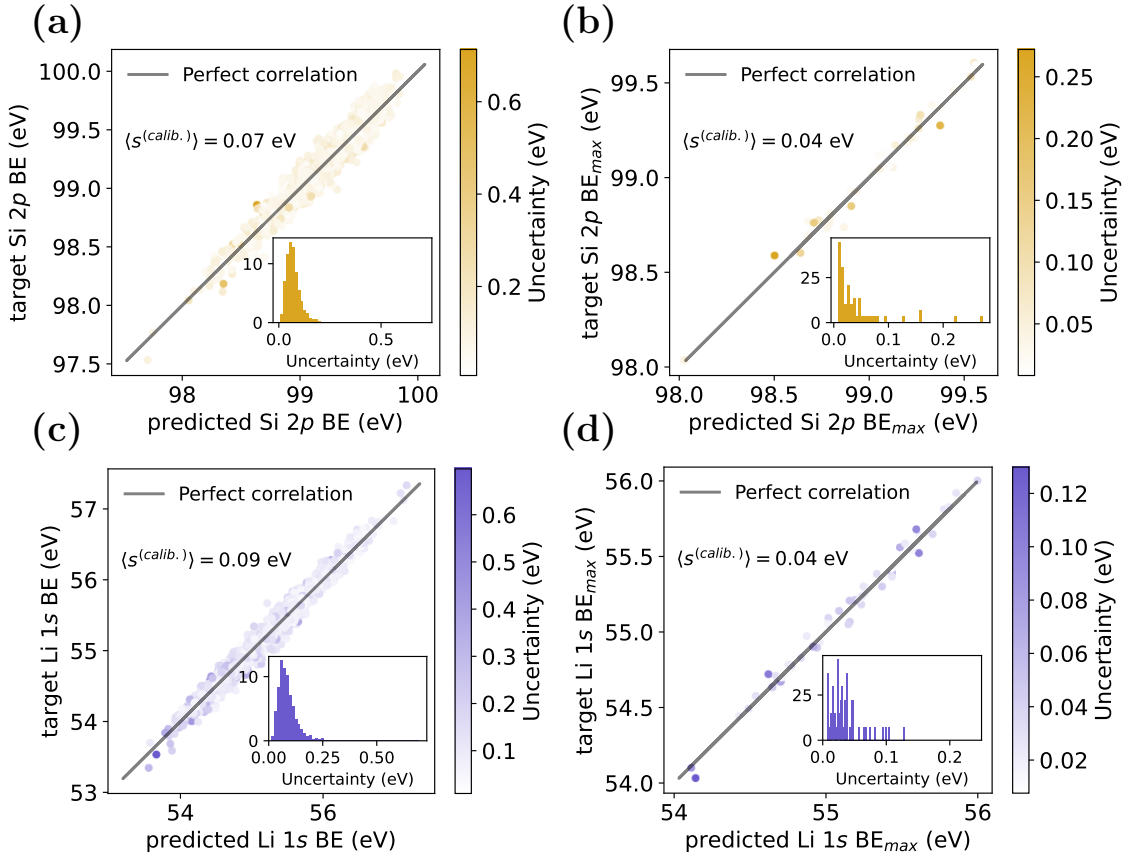


Figure 3: Uncertainty estimates for the BE (a,c) and BE<sub>max</sub> (b,d) predictions on the validation set. (a) and (b) panels correspond to the Si 2p level, while (c) and (d) show results for the Li 1s level. Each plot reports the average calibrated uncertainty  $\langle s^{(calib.)} \rangle$ , and the insets display histograms of the corresponding uncertainty distributions.

an abrupt shift in the Si 2*p* BE was observed and attributed to the phase transition between c-Li<sub>3.75</sub>Si and a-Li<sub>*x*</sub>Si, reflecting structural and electronic changes during cycling.<sup>11</sup> Collectively, these studies provide XPS benchmarks for the stoichiometric and structural evolution of Si-based electrodes upon cycling, against which ML-predicted BEs and spectral trends can be directly assessed.

Building on these experimental benchmarks, a first attempt to construct a stoichiometry map for the discharge of a Si electrode was carried out by applying the ML model to the complete Li<sub>*x*</sub>Si dataset<sup>93</sup> (see Figure S2, Supporting Information). The predicted BE<sub>max</sub> values show no clear dependence on Li concentration for the Li 1*s* core-level, whereas the Si 2*p*<sup>3/2</sup> BE exhibits an upward trend with decreasing Li content, as expected upon delithiation. Moreover, the standard deviation of BE<sub>max</sub> in the dataset is relatively small at low Li concentrations, but increases substantially for *x* > 1.5. This is partly attributable to the diversity of local atomic environments in the dataset, beneficial for training a MLIP, but which includes motifs unlikely to occur under galvanostatic cycling conditions. In addition, amorphous structures at high Li concentrations are underrepresented, further contributing to the increased uncertainty. These observations highlight the need to generate additional, physically relevant structures, in particular a-Li<sub>*x*</sub>Si configurations.

### Generation of amorphous Li<sub>*x*</sub>Si structures

To generate realistic Li<sub>*x*</sub>Si amorphous structures, both near-equilibrium and compositionally driven configurations were prepared, following the protocols detailed in the Methods Section. The near-equilibrium amorphous structures were generated using the melt-quench-anneal (MQA) procedure described in Ref. 100, with stoichiometries ranging from *x*=0 to 4.4 in a 76000-atom supercell. The compositionally driven structures were instead generated using grand canonical Monte Carlo (GCMC) simulations<sup>101</sup> coupled with MD to address the delithiation process. We considered as starting points different crystalline phases with variable initial compositions, namely c-Li<sub>3.75</sub>Si, (a-)c-Li<sub>4.4</sub>Si, c-Li<sub>3.25</sub>Si and c-Li<sub>1.7</sub>Si, using

supercells containing 76000, 76000, 58752 and 27360 atoms, respectively. The metastable phase  $c\text{-Li}_{3.75}\text{Si}$  is included as it is the key crystalline compound formed electrochemically when  $a\text{-Li}_x\text{Si}$  reaches a critical concentration,<sup>22,25,26</sup> while the other crystalline phases, taken from the equilibrium Li-Si phase diagram,<sup>110</sup> serve as structural references to characterize the evolution of  $\text{Li}_x\text{Si}$ . An amorphous configuration ( $a\text{-Li}_{4.4}\text{Si}$ ) was also studied to isolate the effects of structural order on the delithiation mechanism and the resulting XPS spectrum.

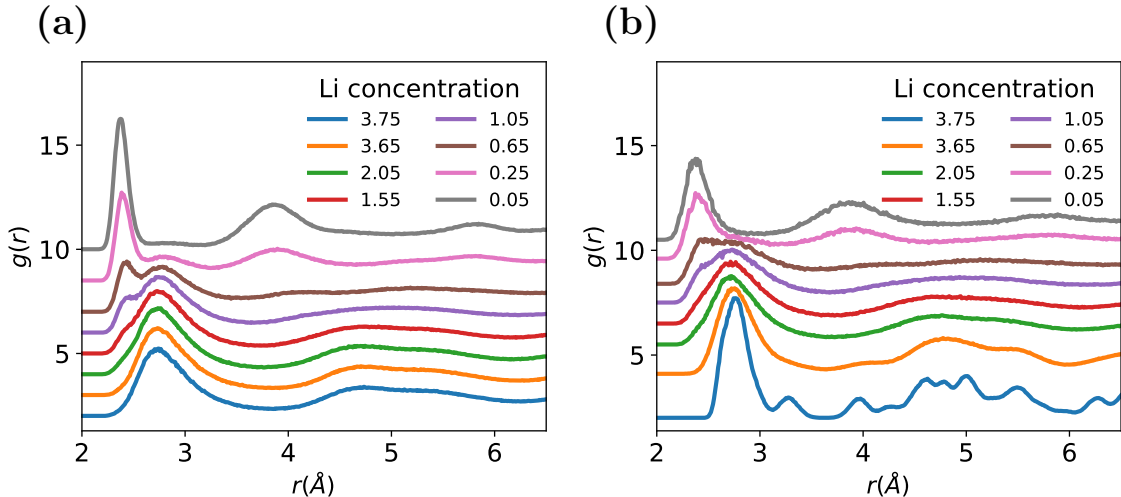


Figure 4: Radial distribution functions (RDFs) at 300 K of the structures generated using a melt-quench-anneal procedure (a) and a grand canonical Monte Carlo simulation starting from  $c\text{-Li}_{3.75}\text{Si}$  (b).

In Figure 4, the radial distribution functions (RDFs) of the generated structures are shown, comparing those obtained with the MQA procedure (a) and the GCMC-based delithiation protocol starting from  $c\text{-Li}_{3.75}\text{Si}$  (b) at different Li concentrations. Both methods display broadened features and attenuation of long-range order, consistent with disordered atomic environments, except in the vicinity of  $x = 3.75$ , where the structures generated with GCMC show coexistence of crystalline and amorphous features. By combining MQA and GCMC, the dataset achieves broader coverage, with MQA providing amorphous environments across concentrations and GCMC capturing metastable or partially ordered motifs relevant to early delithiation.

Convergence tests were carried out on the BE values computed along the GCMC trajec-

tories by considering the number of MD steps per MC move, the acceptance ratio and the system size (see Figure S3, Supporting Information). No significant changes were observed in the predicted BE values with respect to the first two parameters, while a dependence on the system size is observed, with convergence achieved only for systems containing at least 8000 Si atoms (within an initial  $\text{Li}_{3.75}\text{Si}$  cell of 76000 atoms). These sizes clearly exceeds the practical limits of conventional DFT-based simulations, further supporting the suitability of the ML approach for efficiently predicting XPS-related properties in realistic Li–Si systems.

### Li 1s spectrum and voltage profile during $\text{Li}_x\text{Si}$ delithiation

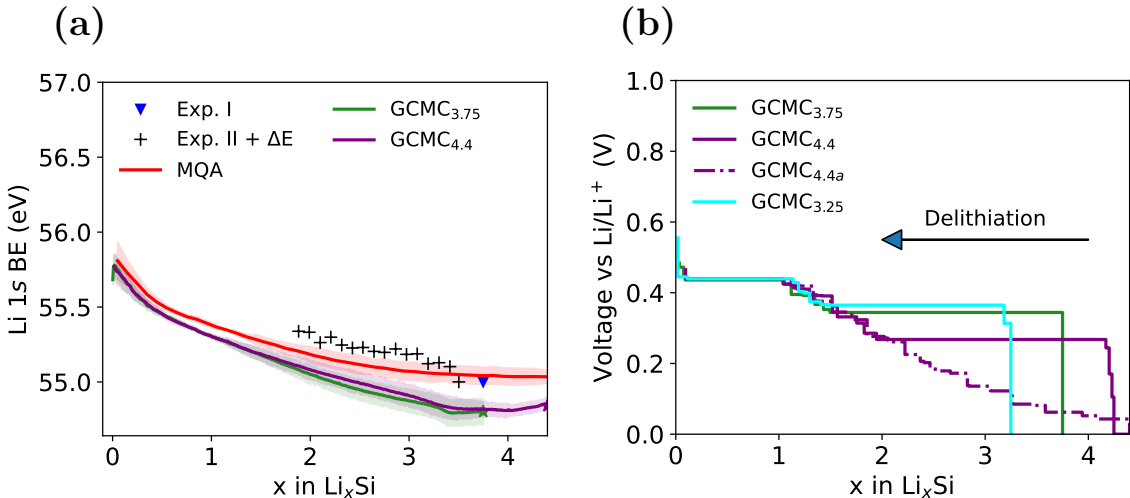


Figure 5: (a) Stoichiometry map showing the peak position of Li 1s for  $\text{Li}_x\text{Si}$  structures generated using MQA (red) and GCMC simulations starting from c- $\text{Li}_{3.75}\text{Si}$  (green) and c- $\text{Li}_{4.4}\text{Si}$  (purple), compared to experimental data corresponding to the delithiation of Si electrodes (black crosses and blue triangles). The stars represent the values for the initial structure in the GCMC simulations and the shaded regions correspond to the predicted uncertainties. (b) Delithiation voltage curves from GCMC simulations starting from c- $\text{Li}_{3.75}\text{Si}$  (green), c- $\text{Li}_{4.4}\text{Si}$  (purple), a- $\text{Li}_{4.4}\text{Si}$  (purple dashed) and c- $\text{Li}_{3.25}\text{Si}$  (cyan).

The ML model was applied to the  $\text{Li}_x\text{Si}$  structures generated using MQA and GCMC, and the resulting Li 1s BEs are compared in Figure 5(a). The peak positions obtained from MQA structures (red solid line) and GCMC simulations starting from c- $\text{Li}_{3.75}\text{Si}$  (green solid line) and c- $\text{Li}_{4.4}\text{Si}$  (purple solid line) are consistent with experimental measurements

of Si electrode delithiation, where the first dataset (black crosses) was extracted from Ref. 11 and the second dataset (blue triangles) from Ref. 109. To align the two experimental datasets, the energies of the first dataset (black crosses) were rigidly shifted by  $\Delta E = 2.86$  eV. Details of the data extraction, spectral fitting, and alignment procedures are provided in the Supporting Information (Figure S4). Both simulation protocols reproduce the experimentally observed downshift of the Li 1s binding energy with increasing Li concentration. However, the GCMC results are systematically shifted to slightly lower binding energies compared to MQA. The corresponding delithiation voltage curves, shown in Figure 5(b), were obtained from the GCMC-generated structures, including those derived from c-Li<sub>3.75</sub>Si (green), c-Li<sub>4.4</sub>Si (purple), a-Li<sub>4.4</sub>Si (purple dashed), and c-Li<sub>3.25</sub>Si (cyan). These curves were constructed by neglecting the enthalpic and entropic contributions to the Gibbs free energy. Under this approximation, the voltage relative to Li/Li<sup>+</sup> for a transition between two phases of Li<sub>x</sub>Si can be expressed as<sup>111–113</sup>

$$eV(x) \approx -\frac{E_f(x + \Delta x) - E_f(x)}{\Delta x}, \quad (10)$$

with

$$E_f(x) = E_{\text{Li}_x\text{Si}} - xE_{\text{Li}} - E_{\text{Si}}, \quad (11)$$

where  $E_f$  denotes the formation energy per Si atom in eV,  $E_{\text{Li}_x\text{Si}}$  is the total energy per Si atom of the Li<sub>x</sub>Si phase,  $E_{\text{Li}}$  the total energy per atom of BCC lithium, and  $E_{\text{Si}}$  the total energy per atom of amorphous silicon. In Equation 10, the formation energy is evaluated at the vertices of the convex hull constructed from the  $E_f(x)$  curve (see Figure S5, Supporting Information). The figure shows that delithiation of c-Li<sub>x</sub>Si proceeds through a two-phase mechanism, manifested as a voltage plateau that connects the initial crystalline and final amorphous phases of Li<sub>x</sub>Si. The estimated plateau voltages are 0.27 V for c-Li<sub>4.4</sub>Si, 0.34 V for c-Li<sub>3.75</sub>Si, and 0.36 V for c-Li<sub>3.25</sub>Si. For c-Li<sub>3.75</sub>Si, our computed plateau voltage falls within

the lower end of experimentally reported values (0.38–0.45 V),<sup>24,32,33,114–116</sup> and is consistent with previous theoretical predictions of 0.27 V.<sup>93</sup> These plateaus provide insight into the sequence in which the c-Li<sub>x</sub>Si phases undergo delithiation. In contrast, the a-Li<sub>4.4</sub>Si begins delithiation at voltages substantially lower than those of the crystalline phases, indicating that lithium is preferentially extracted from the amorphous environments rather than from the crystalline ones.

### Stoichiometry map for Si $2p^{3/2}$ BE<sub>max</sub> in Li<sub>x</sub>Si

Figure 6(a) shows the stoichiometry maps for the Si  $2p^{3/2}$  BE<sub>max</sub>. In the low Li concentration regime, where a-Li<sub>x</sub>Si phases dominate, the Si  $2p^{3/2}$  BEs resulting from the MQA (red solid line) and GCMC (green and purple solid lines) structures yield similar results, which are also comparable to experiments obtained either under *operando*<sup>11</sup> (black crosses) or *ex situ*<sup>109</sup> (blue triangles) conditions. At higher Li contents, the predictions of the ML model for the GCMC-generated structures obtained from c-Li<sub>4.4</sub>Si and c-Li<sub>3.75</sub>Si, align more closely with the *ex situ* measurements, where the experimentally observed downshift in BE at increasing  $x$  is quantitatively well reproduced. It is worth noting that, as for the Li  $1s$  spectrum, the experimental dataset corresponding to the black crosses was rigidly shifted to align with *ex situ* data in the low-lithiation regime ( $\Delta E = 1.8$  eV, see Supporting Information for the details). Despite this alignment, the two experimental datasets show a discrepancy of up to  $\sim 1$  eV in BE<sub>max</sub> for  $x > 1.7$ , which may arise from the different calibration approaches or from other experimental factors not accounted for in our model.<sup>117</sup>

Interestingly, at the onset of delithiation, a pronounced downshift in the Si  $2p^{3/2}$  BE<sub>max</sub> is observed for the GCMC simulations initiated from c-Li<sub>3.75</sub>Si and c-Li<sub>4.4</sub>Si, which is subsequently reversed around  $x \approx 3.4$ . These dips are observed exclusively when GCMC simulations use crystalline phases as initial configurations. As shown in Figure 7, benchmark calculations performed starting from crystalline and amorphous phases having the same Si  $2p^{3/2}$  BE<sub>max</sub>, namely Li<sub>4.4</sub>Si and Li<sub>1.7</sub>Si, evidence that the reversal in the BE<sub>max</sub> trend is a

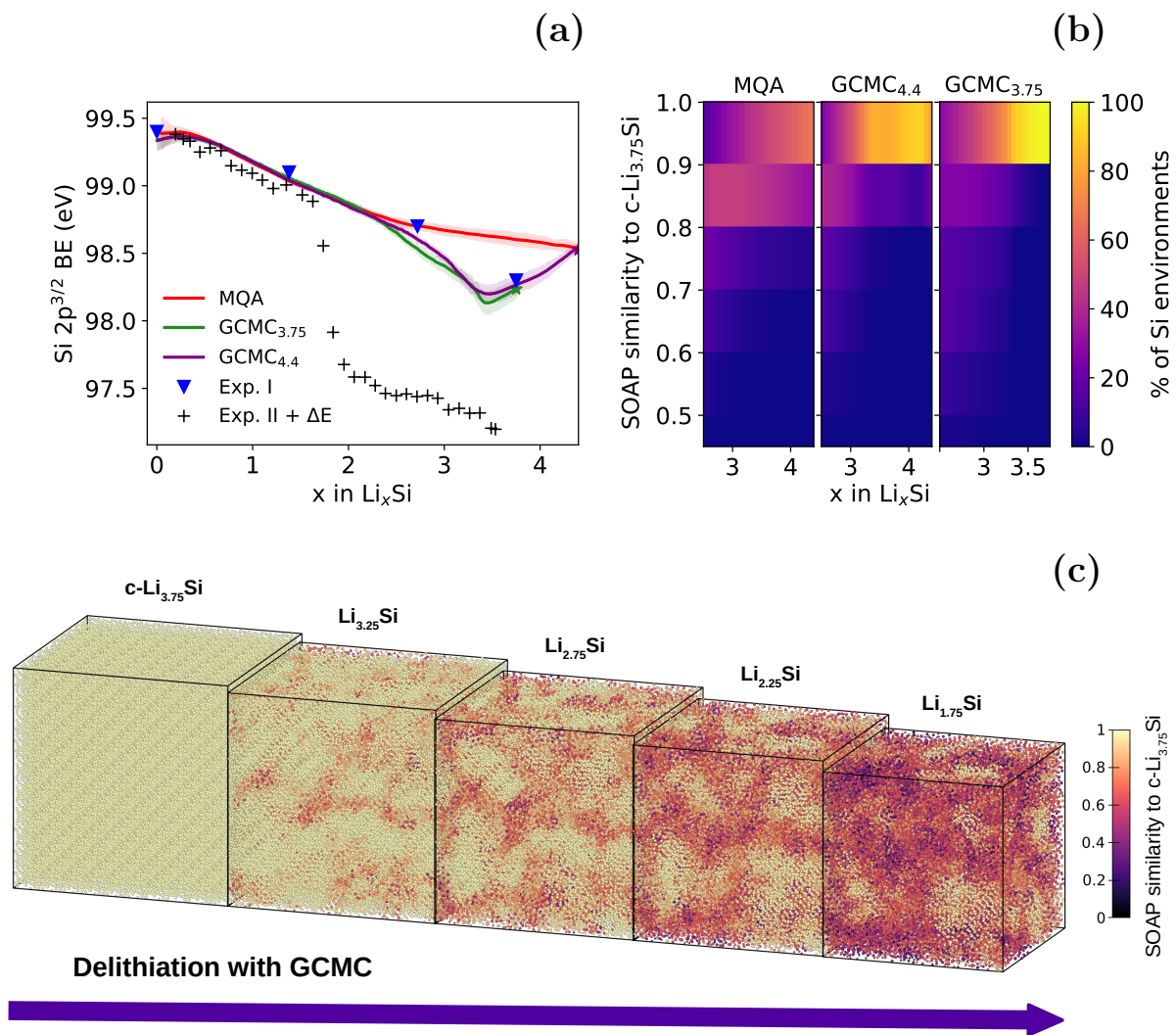


Figure 6: (a) Stoichiometry maps showing the peak position of Si  $2p^{3/2}$  for  $\text{Li}_x\text{Si}$  structures generated using MQA (red) and GCMC starting from  $c\text{-Li}_{3.75}\text{Si}$  (green) and  $c\text{-Li}_{4.4}\text{Si}$  (purple), compared to experimental data from Si electrodes obtained in *operando* (black crosses) and *ex situ* (blue triangles). The stars represent the values for the initial structure in the GCMC simulations and the shaded regions correspond to the predicted uncertainties. (b) Heat map showing the SOAP similarity between Si environments generated via MQA and GCMC and those in  $c\text{-Li}_{3.75}\text{Si}$ . The color scale represents the percentage of Si environments at a given stoichiometry that exhibit a specific SOAP similarity to  $c\text{-Li}_{3.75}\text{Si}$ . (c) Simulation snapshots of  $\text{Li}_x\text{Si}$  structures obtained during the delithiation of  $c\text{-Li}_{3.75}\text{Si}$  using GCMC. The color map accounts for the SOAP similarity of each local environment to  $c\text{-Li}_{3.75}\text{Si}$ .

characteristic of the trajectories initiated from the crystalline phases, indicating that this behavior originates from the crystal-to-amorphous transition. Hence, this kind of evolution observed in  $BE_{\max}$  during early delithiation can be interpreted as the spectroscopic manifestation of the structural disordering process captured by XPS (for the effects on the FWHM, see Figure S6 in Supporting Information). In particular, the Si  $2p^{3/2}$  core level demonstrates greater sensitivity to this transition than the Li  $1s$ , highlighting its effectiveness as a probe of structural evolution.

To support the analysis presented in the stoichiometry map, a SOAP similarity analysis was carried out, taking  $c\text{-Li}_{3.75}\text{Si}$  as the reference system (see Figure 6 (b) and (c) panels). The heat map (b) displays the percentage of Si environments that exhibit a specific SOAP similarity to the reference system  $c\text{-Li}_{3.75}\text{Si}$ , comparing structures generated via MQA and GCMC. While for MQA the fraction of structures with similarity above 0.9 never exceeds 65% at any concentration, consistent with their amorphous character, in the GCMC simulations starting from both  $c\text{-Li}_{3.75}\text{Si}$  and  $c\text{-Li}_{4.4}\text{Si}$ , the percentage stay above 90% and 77%, respectively, up to  $x = 3.3$ , indicating the presence of a large fraction of crystalline domains. This can be also seen in Figure 6(c), where few simulation snapshots are presented for the delithiation of  $c\text{-Li}_{3.75}\text{Si}$  using GCMC, where the color map accounts for the SOAP similarity of each local environment to  $c\text{-Li}_{3.75}\text{Si}$ . This analysis further reveals that delithiation proceeds in a non-uniform manner, with clusters of  $c\text{-Li}_{3.75}\text{Si}$  environments persisting even as the average composition (b) evolves toward amorphous states. These residual crystalline domains prevent complete Li extraction and thus provide a microscopic explanation for the irreversible capacity loss typically observed in Si-based anodes. Similar signatures of persistent structural motifs during  $c\text{-Li}_{3.75}\text{Si}$  delithiation have been reported previously in experimental studies<sup>118–120</sup> and in MD simulations.<sup>93,121</sup> Fu et al.,<sup>93</sup> for example, observed that the  $c\text{-Li}_{3.75}\text{Si}$  lattice remains largely crystalline down to  $c\text{-Li}_{3.0}\text{Si}$ , with limited formation of Si–Si dimers and Si–Si–Si motifs, in agreement with earlier analyses of Li-deficient  $c\text{-Li}_{3.75-\delta}\text{Si}$ .<sup>32</sup> However, the simulation cell size used in that study (608 atoms) precluded the

resolution of spatially heterogeneous crystalline domains. In contrast, the large-scale simulations used here (76000 atoms) enable direct visualization of these persistent crystalline clusters providing new insight into their spatial distribution, evolution and connect these structural motifs with the changes observed in the Si  $2p^{3/2}$  XPS spectrum.

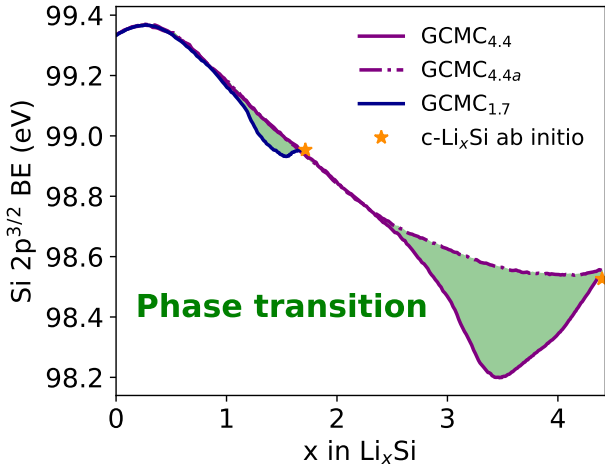


Figure 7: Stoichiometry maps for Si  $2p^{3/2}$   $BE_{\max}$  for  $Li_xSi$  structures generated using GCMC starting from c- $Li_{4.4}Si$  (purple), a- $Li_{4.4}Si$  (purple dashed) and c- $Li_{1.7}Si$  (dark blue). The values for the initial crystalline structures are represented with orange stars, while the shaded region accounts for the crystal-amorphous phase transition

## Conclusions

In this work, we have introduced a machine-learning framework that enables accurate, scalable, and uncertainty-aware prediction of core-level XPS binding energies in structurally complex  $Li_xSi$  systems, overcoming the prohibitive cost of conventional *ab initio* approaches. Our model achieves near-DFT accuracy for Li  $1s$  and Si  $2p$  levels while remaining computationally efficient for large, amorphous configurations. The calibrated uncertainty estimates fall within typical experimental XPS resolution, providing confidence in the robustness of the predictions. Applying the model to extensive melt-quench-anneal and grand-canonical Monte Carlo simulations allowed us to construct stoichiometry maps that quantitatively link XPS peak positions to lithium content and structural evolution during (de)lithiation. Compari-

son with *operando* and *ex situ* experimental data shows excellent agreement. This analysis also reveals clear spectroscopic signatures of the crystalline-to-amorphous transition and the persistence of crystalline domains during early delithiation, offering microscopic insight into irreversible capacity loss in Si anodes. More broadly, this work establishes a general, transferable strategy for coupling machine learning, large-scale atomistic simulations, and XPS, to enable quantitative interpretation of spectroscopic data in disordered battery materials under realistic operating conditions.

## Acknowledgement

This work was partly supported by the European Union’s Horizon 2020 research and innovation programme (BIG-MAP, Grant No. 957189, also part of the BATTERY 2030+ initiative, Grant No. 957213), by the European High Performance Computing Joint Undertaking (MaX Centre of Excellence – Materials design at the eXascale, program HORIZON-EUROHPC-JU-2021-COE01, Grant No. 101093374), and by the European Union – NextGenerationEU, through the MUR – Prin 2022 programme (2D-FRONTIERS, Grant No. 20228879FT). DT and MC acknowledge support from a Sinergia grant of the Swiss National Science Foundation (grant ID CRSII5\_202296). MC acknowledges support from the European Research Council (ERC) under the research and innovation program (Grant Agreement No. 101001890-FIAMMA) and the NCCR MARVEL, funded by the Swiss National Science Foundation (SNSF, Grant No. 205602). The authors acknowledge the CINECA award under the ISCRA initiative, for the availability of high-performance computing resources and support.

## Supporting Information Available

Details on: model hyperparameters and learning curves; model evaluation on the  $\text{Li}_x$  DFT dataset; parameter convergence and formation energies from GCMC simulations; XPS data processing and alignment.

## References

- (1) Weiland, C.; Rumaiz, A.; Lysaght, P.; Karlin, B.; Woicik, J. et al. NIST high throughput variable kinetic energy hard X-ray photoelectron spectroscopy facility. *Journal of Electron Spectroscopy and Related Phenomena* **2013**, *190*, 193–200.
- (2) Woicik, J. C.; Woicik, J. *Hard X-ray photoelectron spectroscopy (HAXPES)*; Springer, 2016; Vol. 59.
- (3) Fehse, M.; Iadecola, A.; Simonelli, L.; Longo, A.; Stievano, L. The rise of X-ray spectroscopies for unveiling the functional mechanisms in batteries. *Phys. Chem. Chem. Phys.* **2021**, *23*, 23445–23465.
- (4) Axnanda, S.; Crumlin, E. J.; Mao, B.; Rani, S.; Chang, R. et al. Using "Tender" X-ray Ambient Pressure X-Ray Photoelectron Spectroscopy as A Direct Probe of Solid-Liquid Interface. *Scientific reports* **2015**, *5*, 9788.
- (5) Zhu, S.; Scardamaglia, M.; Kundsén, J.; Sankari, R.; Tarawneh, H. et al. HIPPIE: a new platform for ambient-pressure X-ray photoelectron spectroscopy at the MAX IV Laboratory. *Synchrotron Radiation* **2021**, *28*, 624–636.
- (6) Manthiram, A.; Yu, X.; Wang, S. Lithium battery chemistries enabled by solid-state electrolytes. *Nature Reviews Materials* **2017**, *2*, 1–16.
- (7) Wenzel, S.; Leichtweiss, T.; Krüger, D.; Sann, J.; Janek, J. Interphase formation on lithium solid electrolytes—An in situ approach to study interfacial reactions by photoelectron spectroscopy. *Solid State Ionics* **2015**, *278*, 98–105.
- (8) Favaro, M.; Abdi, F. F.; Crumlin, E. J.; Liu, Z.; van de Krol, R. et al. Interface Science Using Ambient Pressure Hard X-ray Photoelectron Spectroscopy. *Surfaces* **2019**, *2*, 78–99.

- (9) Kiuchi, H.; Hikima, K.; Shimizu, K.; Kanno, R.; Toshiharu, F. et al. Operando hard X-ray photoelectron spectroscopy of LiCoO<sub>2</sub> thin film in an all-solid-state lithium ion battery. *Electrochemistry Communications* **2020**, *118*, 106790.
- (10) Mirolo, M.; Wu, X.; Vaz, C. A.; Novák, P.; El Kazzi, M. Unveiling the complex redox reactions of SnO<sub>2</sub> in Li-ion batteries using operando X-ray photoelectron spectroscopy and in situ X-ray absorption spectroscopy. *ACS Applied Materials & Interfaces* **2021**, *13*, 2547–2557.
- (11) Endo, R.; Ohnishi, T.; Takada, K.; Masuda, T. Electrochemical Lithiation and Delithiation in Amorphous Si Thin Film Electrodes Studied by Operando X-ray Photoelectron Spectroscopy. *The Journal of Physical Chemistry Letters* **2022**, *13*, 7363–7370.
- (12) Philippe, B.; Dedryvère, R.; Allouche, J.; Lindgren, F.; Gorgoi, M. et al. Nanosilicon Electrodes for Lithium-Ion Batteries: Interfacial Mechanisms Studied by Hard and Soft X-ray Photoelectron Spectroscopy. *Chemistry of Materials* **2012**, *24*, 1107–1115.
- (13) Sachs, M.; Gellert, M.; Chen, M.; Drescher, H.-J.; Kachel, S. R. et al. LiNi<sub>0.5</sub>Mn<sub>1.5</sub>O<sub>4</sub> high-voltage cathode coated with Li<sub>4</sub>Ti<sub>5</sub>O<sub>12</sub>: a hard X-ray photoelectron spectroscopy (HAXPES) study. *Physical Chemistry Chemical Physics* **2015**, *17*, 31790–31800.
- (14) Assat, G.; Foix, D.; Delacourt, C.; Iadecola, A.; Dedryvère, R. et al. Fundamental interplay between anionic/cationic redox governing the kinetics and thermodynamics of lithium-rich cathodes. *Nature communications* **2017**, *8*, 2219.
- (15) Wu, X.; Villevieille, C.; Novák, P.; El Kazzi, M. Monitoring the chemical and electronic properties of electrolyte–electrode interfaces in all-solid-state batteries using operando X-ray photoelectron spectroscopy. *Physical Chemistry Chemical Physics* **2018**, *20*, 11123–11129.

- (16) Wu, H.; Cui, Y. Designing nanostructured Si anodes for high energy lithium ion batteries. *Nano today* **2012**, *7*, 414–429.
- (17) Taiwo, O. O.; Loveridge, M.; Beattie, S. D.; Finegan, D. P.; Bhagat, R. et al. Investigation of cycling-induced microstructural degradation in silicon-based electrodes in lithium-ion batteries using X-ray nanotomography. *Electrochim. Acta* **2017**, *253*, 85–92.
- (18) Müller, S.; Pietsch, P.; Brandt, B.-E.; Baade, P.; De Andrade, V. et al. Quantification and modeling of mechanical degradation in lithium-ion batteries based on nanoscale imaging. *Nature Commun.* **2018**, *9*, 2340.
- (19) Müller, S.; Lippuner, M.; Verezhak, M.; De Andrade, V.; De Carlo, F. et al. Multimodal Nanoscale Tomographic Imaging for Battery Electrodes. *Adv. Energy Mater.* **2020**, *10*, 1904119.
- (20) Domi, Y.; Usui, H.; Yamaguchi, K.; Yodoya, S.; Sakaguchi, H. Silicon-based anodes with long cycle life for lithium-ion batteries achieved by significant suppression of their volume expansion in ionic-liquid electrolyte. *ACS Applied Materials & Interfaces* **2019**, *11*, 2950–2960.
- (21) Domi, Y.; Usui, H.; Ando, A.; Nishikawa, K.; Sakaguchi, H. Analysis of the Li distribution in Si-based negative electrodes for lithium-ion batteries by soft X-ray emission spectroscopy. *ACS Applied Energy Materials* **2020**, *3*, 8619–8626.
- (22) Obrovac, M.; Christensen, L. Structural changes in silicon anodes during lithium insertion/extraction. *Electrochemical and solid-state letters* **2004**, *7*, A93.
- (23) Rohrer, J.; Albe, K. Insights into degradation of Si anodes from first-principle calculations. *The Journal of Physical Chemistry C* **2013**, *117*, 18796–18803.

- (24) Gao, H.; Xiao, L.; Plümel, I.; Xu, G.-L.; Ren, Y. et al. Parasitic Reactions in Nanosized Silicon Anodes for Lithium-Ion Batteries. *Nano Letters* **2017**, *17*, 1512–1519, PMID: 28177638.
- (25) Hatchard, T. D.; Dahn, J. R. In Situ XRD and Electrochemical Study of the Reaction of Lithium with Amorphous Silicon. *Journal of The Electrochemical Society* **2004**, *151*, A838.
- (26) Li, J.; Dahn, J. An in situ X-ray diffraction study of the reaction of Li with crystalline Si. *Journal of The Electrochemical Society* **2007**, *154*, A156.
- (27) Misra, S.; Liu, N.; Nelson, J.; Hong, S. S.; Cui, Y. et al. In situ X-ray diffraction studies of (de) lithiation mechanism in silicon nanowire anodes. *Acs Nano* **2012**, *6*, 5465–5473.
- (28) Wang, C.-M.; Li, X.; Wang, Z.; Xu, W.; Liu, J. et al. In Situ TEM Investigation of Congruent Phase Transition and Structural Evolution of Nanostructured Silicon/Carbon Anode for Lithium Ion Batteries. *Nano Letters* **2012**, *12*, 1624–1632, PMID: 22385150.
- (29) Liu, X. H.; Wang, J. W.; Huang, S.; Fan, F.; Huang, X. et al. In situ atomic-scale imaging of electrochemical lithiation in silicon. *Nature Nanotechnology* **2012**, *7*, 749–756.
- (30) Gu, M.; Wang, Z.; Connell, J. G.; Perea, D. E.; Lauthon, L. J. et al. Electronic origin for the phase transition from amorphous  $\text{Li}_x\text{Si}$  to crystalline  $\text{Li}_{15}\text{Si}_4$ . *ACS nano* **2013**, *7*, 6303–6309.
- (31) Key, B.; Bhattacharyya, R.; Morcrette, M.; Seznec, V.; Tarascon, J.-M. et al. Real-time NMR investigations of structural changes in silicon electrodes for lithium-ion batteries. *Journal of the American Chemical Society* **2009**, *131*, 9239–9249.

- (32) Ogata, K.; Salager, E.; Kerr, C.; Fraser, A.; Ducati, C. et al. Revealing lithium–silicide phase transformations in nano-structured silicon-based lithium ion batteries via in situ NMR spectroscopy. *Nature communications* **2014**, *5*, 3217.
- (33) Kitada, K.; Pecher, O.; Magusin, P. C. M. M.; Groh, M. F.; Weatherup, R. S. et al. Unraveling the Reaction Mechanisms of SiO Anodes for Li-Ion Batteries by Combining in Situ  $^7\text{Li}$  and ex Situ  $^7\text{Li}/^{29}\text{Si}$  Solid-State NMR Spectroscopy. *Journal of the American Chemical Society* **2019**, *141*, 7014–7027, PMID: 30964666.
- (34) Smith, M.; Scudiero, L.; Espinal, J.; McEwen, J.-S.; Garcia-Perez, M. Improving the deconvolution and interpretation of XPS spectra from chars by ab initio calculations. *Carbon* **2016**, *110*, 155–171.
- (35) Trinh, Q. T.; Bhola, K.; Amaniampong, P. N.; Jerome, F.; Mushrif, S. H. Synergistic application of XPS and DFT to investigate metal oxide surface catalysis. *The Journal of Physical Chemistry C* **2018**, *122*, 22397–22406.
- (36) Yu, J.; Zhang, H.; Olsson, E.; Yu, T.; Liu, Z. et al. A novel amorphous P4SSe2 compound as an advanced anode for sodium-ion batteries in ether-based electrolytes. *J. Mater. Chem. A* **2021**, *9*, 12029–12040.
- (37) Takatani, S.; Takeshi Kikawa, T. K.; Masatoshi Nakazawa, M. N. Amorphous-Se/GaAs –A Novel Heterostructure for Solid-State Devices–. *Japanese Journal of Applied Physics* **1991**, *30*, 3763.
- (38) Saito, K.; Mori, T.; Orikasa, Y.; Hakari, T.; Deguchi, M. et al. X-Ray Absorption Spectroscopic Analysis of Li<sub>3</sub>PS<sub>4</sub> Glass-Carbon Composite Cathodes for All-Solid-State Lithium Secondary Battery. *ECS Meeting Abstracts* **2016**, *MA2016-02*, 4050.
- (39) Wang, Z.; hua Luo, S.; Zhang, X.; Guo, S.; Li, P. et al. Glass and glass ceramic electrodes and solid electrolyte materials for lithium ion batteries: A review. *Journal of Non-Crystalline Solids* **2023**, *619*, 122581.

- (40) Tatsumisago, M.; Hayashi, A. Superionic glasses and glass–ceramics in the Li<sub>2</sub>S–P<sub>2</sub>S<sub>5</sub> system for all-solid-state lithium secondary batteries. *Solid State Ionics* **2012**, *225*, 342–345, Solid State Ionics 18 Proceedings of the 18th International Conference on Solid State Ionics Warsaw, Poland, July 3 -8, 2011.
- (41) Schmidt, J.; Marques, M. R. G.; Botti, S.; Marques, M. A. L. Recent advances and applications of machine learning in solid-state materials science. *npj Computational Materials* **2019**, *5*, 83.
- (42) Bartók, A. P.; De, S.; Poelking, C.; Bernstein, N.; Kermode, J. R. et al. Machine learning unifies the modeling of materials and molecules. *Science Advances* **2017**, *3*, e1701816.
- (43) Deringer, V. L.; Bartók, A. P.; Bernstein, N.; Wilkins, D. M.; Ceriotti, M. et al. Gaussian Process Regression for Materials and Molecules. *Chemical Reviews* **2021**, *121*, 10073–10141.
- (44) Batatia, I.; Kovacs, D. P.; Simm, G.; Ortner, C.; Csanyi, G. MACE: Higher Order Equivariant Message Passing Neural Networks for Fast and Accurate Force Fields. *Advances in Neural Information Processing Systems*. 2022; pp 11423–11436.
- (45) Wang, H.; Zhang, L.; Han, J.; E, W. DeePMD-kit: A deep learning package for many-body potential energy representation and molecular dynamics. *Computer Physics Communications* **2018**, *228*, 178–184.
- (46) Zeng, J.; Zhang, D.; Lu, D.; Mo, P.; Li, Z. et al. DeePMD-kit v2: A software package for deep potential models. *The Journal of Chemical Physics* **2023**, *159*, 054801.
- (47) Bartók, A. P.; Payne, M. C.; Kondor, R.; Csányi, G. Gaussian Approximation Potentials: The Accuracy of Quantum Mechanics, without the Electrons. *Physical Review Letters* **2010**, *104*, 136403.

- (48) Behler, J.; Parrinello, M. Generalized Neural-Network Representation of High-Dimensional Potential-Energy Surfaces. *Physical Review Letters* **2007**, *98*, 146401.
- (49) Smith, J. S.; Isayev, O.; Roitberg, A. E. ANI-1: an extensible neural network potential with DFT accuracy at force field computational cost. *Chemical Science* **2017**, *8*, 3192–3203.
- (50) Schütt, K. T.; Hessmann, S. S. P.; Gebauer, N. W. A.; Lederer, J.; Gastegger, M. SchNetPack 2.0: A neural network toolbox for atomistic machine learning. *The Journal of Chemical Physics* **2023**, *158*, 144801.
- (51) Rupp, M.; Tkatchenko, A.; Müller, K.-R.; von Lilienfeld, O. A. Fast and Accurate Modeling of Molecular Atomization Energies with Machine Learning. *Physical Review Letters* **2012**, *108*, 058301.
- (52) Butler, K. T.; Davies, D. W.; Cartwright, H.; Isayev, O.; Walsh, A. Machine learning for molecular and materials science. *Nature* **2018**, *559*, 547–555.
- (53) Ko, T. W.; Finkler, J. A.; Goedecker, S.; Behler, J. A fourth-generation high-dimensional neural network potential with accurate electrostatics including non-local charge transfer. *Nature Communications* **2021**, *12*, 398.
- (54) Unke, O. T.; Meuwly, M. PhysNet: A Neural Network for Predicting Energies, Forces, Dipole Moments, and Partial Charges. *Journal of Chemical Theory and Computation* **2019**, *15*, 3678–3693.
- (55) Batzner, S.; Musaelian, A.; Sun, L.; Geiger, M.; Mailoa, J. P. et al. E(3)-equivariant graph neural networks for data-efficient and accurate interatomic potentials. *Nat. Commun.* **2022**, *13*, 2453.
- (56) Fan, Z.; Wang, Y.; Ying, P.; Song, K.; Wang, J. et al. GPUMD: A package for con-

- structuring accurate machine-learned potentials and performing highly efficient atomistic simulations. *The Journal of Chemical Physics* **2022**, *157*, 114801.
- (57) Zeng, J.; Zhang, D.; Peng, A.; Zhang, X.; He, S. et al. DeePMD-kit v3: A Multiple-Backend Framework for Machine Learning Potentials. *Journal of Chemical Theory and Computation* **2025**, *21*, 4375–4385.
- (58) Zhang, L.; Wang, H.; Car, R.; E, W. Phase Diagram of a Deep Potential Water Model. *Phys. Rev. Lett.* **2021**, *126*, 236001.
- (59) Imbalzano, G.; Ceriotti, M. Modeling the Ga/As binary system across temperatures and compositions from first principles. *Phys. Rev. Materials* **2021**, *5*, 063804.
- (60) Lopanitsyna, N.; Ben Mahmoud, C.; Ceriotti, M. Finite-temperature materials modeling from the quantum nuclei to the hot electron regime. *Phys. Rev. Mater.* **2021**, *5*, 043802.
- (61) Gigli, L.; Goscinski, A.; Ceriotti, M.; Tribello, G. A. Modeling the ferroelectric phase transition in barium titanate with DFT accuracy and converged sampling. *Phys. Rev. B* **2024**, *110*, 024101.
- (62) Staacke, C. G.; Huss, T.; Margraf, J. T.; Reuter, K.; Scheurer, C. Tackling Structural Complexity in Li2S-P2S5 Solid-State Electrolytes Using Machine Learning Potentials. *Nanomaterials* **2022**, *12*, 2950.
- (63) Deringer, V. L.; Csányi, G. Machine learning based interatomic potential for amorphous carbon. *Phys. Rev. B* **2017**, *95*, 094203.
- (64) Bartók, A. P.; Kermode, J.; Bernstein, N.; Csányi, G. Machine Learning a General-Purpose Interatomic Potential for Silicon. *Phys. Rev. X* **2018**, *8*, 041048.
- (65) Maresca, F.; Dragoni, D.; Csányi, G.; Marzari, N.; Curtin, W. A. Screw dislocation

- structure and mobility in body centered cubic Fe predicted by a Gaussian Approximation Potential. *npj Computational Materials* **2018**, *4*, 69.
- (66) Deringer, V. L.; Caro, M. A.; Csányi, G. A general-purpose machine-learning force field for bulk and nanostructured phosphorus. *Nature Communications* **2020**, *11*, 5461.
- (67) Deringer, V. L.; Caro, M. A.; Csányi, G. Machine Learning Interatomic Potentials as Emerging Tools for Materials Science. *Advanced Materials* **2019**, *31*, 1902765.
- (68) Rosenbrock, C. W.; Gubaev, K.; Shapeev, A. V.; Pártay, L. B.; Bernstein, N. et al. Machine-learned interatomic potentials for alloys and alloy phase diagrams. *npj Computational Materials* **2021**, *7*, 24.
- (69) Malosso, C.; Zhang, L.; Car, R.; Baroni, S.; Tisi, D. Viscosity in water from first-principles and deep-neural-network simulations. *npj Computational Materials* **2022**, *8*, 139.
- (70) Tisi, D.; Zhang, L.; Bertossa, R.; Wang, H.; Car, R. et al. Heat transport in liquid water from first-principles and deep neural network simulations. *Phys. Rev. B* **2021**, *104*, 224202.
- (71) Tisi, D.; Grasselli, F.; Gigli, L.; Ceriotti, M. Thermal conductivity of  $\text{Li}_3\text{PS}_4$  solid electrolytes with ab initio accuracy. *Phys. Rev. Mater.* **2024**, *8*, 065403.
- (72) Gigli, L.; Tisi, D.; Grasselli, F.; Ceriotti, M. Mechanism of Charge Transport in Lithium Thiophosphate. *Chemistry of Materials* **2024**, *36*, 1482–1496.
- (73) Zhang, L.; Chen, M.; Wu, X.; Wang, H.; E, W. et al. Deep neural network for the dielectric response of insulators. *Phys. Rev. B* **2020**, *102*, 041121.
- (74) Schienbein, P. Spectroscopy from Machine Learning by Accurately Representing the Atomic Polar Tensor. *Journal of Chemical Theory and Computation* **2023**, *19*, 705–712.

- (75) Penfold, T.; Watson, L.; Middleton, C.; David, T.; Verma, S. et al. Machine-Learning Strategies for the Accurate and Efficient Analysis of X-ray Spectroscopy. *Machine Learning: Science and Technology* **2024**,
- (76) Aarva, A.; Deringer, V. L.; Sainio, S.; Laurila, T.; Caro, M. A. Understanding X-ray spectroscopy of carbonaceous materials by combining experiments, density functional theory, and machine learning. Part I: Fingerprint spectra. *Chemistry of Materials* **2019**, *31*, 9243–9255.
- (77) Aarva, A.; Sainio, S.; Deringer, V. L.; Caro, M. A.; Laurila, T. X-ray spectroscopy fingerprints of pristine and functionalized graphene. *The Journal of Physical Chemistry C* **2021**, *125*, 18234–18246.
- (78) Cavagliasso, G.; Chong, D. P. Accurate density-functional calculation of core-electron binding energies by a total-energy difference approach. *The Journal of Chemical Physics* **1999**, *111*, 9485–9492.
- (79) Giannozzi, P.; Baroni, S.; Bonini, N.; Calandra, M.; Car, R. et al. QUANTUM ESPRESSO: a modular and open-source software project for quantum simulations of materials. *Journal of Physics: Condensed Matter* **2009**, *21*, 395502.
- (80) Giannozzi, P.; Andreussi, O.; Brumme, T.; Bunau, O.; Buongiorno Nardelli, M. et al. Advanced capabilities for materials modelling with Quantum ESPRESSO. *Journal of Physics: Condensed Matter* **2017**, *29*, 465901.
- (81) Giannozzi, P.; Baseggio, O.; Bonfà, P.; Brunato, D.; Car, R. et al. Quantum ESPRESSO toward the exascale. *The Journal of Chemical Physics* **2020**, *152*, 154105.
- (82) Prendergast, D.; Galli, G. X-Ray Absorption Spectra of Water from First Principles Calculations. *Phys. Rev. Lett.* **2006**, *96*, 215502.

- (83) Mizoguchi, T.; Tanaka, I.; Gao, S.-P.; Pickard, C. J. First-principles calculation of spectral features, chemical shift and absolute threshold of ELNES and XANES using a plane wave pseudopotential method. *J. Phys. Condens. Matter* **2009**, *21*, 104204.
- (84) Walter, M.; Moseler, M.; Pastewka, L. Offset-corrected  $\Delta$ -Kohn-Sham scheme for semiempirical prediction of absolute x-ray photoelectron energies in molecules and solids. *Phys. Rev. B* **2016**, *94*, 041112.
- (85) Voigt, W. Über das Gesetz der Intensitätsverteilung innerhalb der Linien eines Gasspektrums. *Math.-Phys. Kl. Bayer. Akad. Wis., München* **1912**, 603.
- (86) Prandini, G.; Marrazzo, A.; Castelli, I. E.; Mounet, N.; Marzari, N. Precision and efficiency in solid-state pseudopotential calculations. *npj Comput. Mater.* **2018**, *4*, 72, <http://materialscloud.org/sssp>.
- (87) Murphy, K. P. *Machine learning: a probabilistic perspective*; MIT press, 2012.
- (88) Musil, F.; Willatt, M. J.; Langovoy, M. A.; Ceriotti, M. Fast and accurate uncertainty estimation in chemical machine learning. *Journal of chemical theory and computation* **2019**, *15*, 906–915.
- (89) Grasselli, F.; Chong, S.; Kapil, V.; Bonfanti, S.; Rossi, K. Uncertainty in the era of machine learning for atomistic modeling. *Digital Discovery* **2025**,
- (90) Imbalzano, G.; Zhuang, Y.; Kapil, V.; Rossi, K.; Engel, E. A. et al. Uncertainty estimation for molecular dynamics and sampling. *The Journal of chemical physics* **2021**, *154*, 074102.
- (91) Bartók, A. P.; Kondor, R.; Csányi, G. On representing chemical environments. *Physical Review B—Condensed Matter and Materials Physics* **2013**, *87*, 184115.

- (92) Musil, F.; Veit, M.; Goscinski, A.; Fraux, G.; Willatt, M. J. et al. Efficient implementation of atom-density representations. *The Journal of Chemical Physics* **2021**, *154*, 114109.
- (93) Fu, F.; Wang, X.; Zhang, L.; Yang, Y.; Chen, J. et al. Unraveling the Atomic-scale Mechanism of Phase Transformations and Structural Evolutions during (de)Lithiation in Si Anodes. *Advanced Functional Materials* **2023**, *33*, 2303936.
- (94) Zhang, L.; Han, J.; Wang, H.; Car, R.; E, W. Deep potential molecular dynamics: a scalable model with the accuracy of quantum mechanics. *Physical review letters* **2018**, *120*, 143001.
- (95) Jain, A.; Montoya, J.; Dwaraknath, S.; Zimmermann, N. E. R.; Dagdelen, J. et al. In *Handbook of Materials Modeling: Methods: Theory and Modeling*; Andreoni, W., Yip, S., Eds.; Springer International Publishing: Cham, 2020; pp 1751–1784.
- (96) Eldar, Y.; Lindenbaum, M.; Porat, M.; Zeevi, Y. Y. The farthest point strategy for progressive image sampling. *IEEE transactions on image processing* **1997**, *6*, 1305–1315.
- (97) Seah, M. P. Calibration of electron spectrometer energy scales for AES and XPS. *Journal of Surface Analysis* **2022**, *28*, S30–S32.
- (98) Bernetti, M.; Bussi, G. Pressure control using stochastic cell rescaling. *The Journal of Chemical Physics* **2020**, *153*, 114107.
- (99) Bussi, G.; Donadio, D.; Parrinello, M. Canonical sampling through velocity rescaling. *The Journal of Chemical Physics* **2007**, *126*, 014101.
- (100) Pegolo, P.; Grasselli, F. Thermal transport of glasses via machine learning driven simulations. *Frontiers in Materials* **2024**, *Volume 11 - 2024*.

- (101) Frenkel, D.; Smit, B. *Understanding molecular simulation: from algorithms to applications*; Elsevier, 2023.
- (102) Thompson, A. P.; Aktulga, H. M.; Berger, R.; Bolintineanu, D. S.; Brown, W. M. et al. LAMMPS - a flexible simulation tool for particle-based materials modeling at the atomic, meso, and continuum scales. *Computer Physics Communications* **2022**, *271*, 108171.
- (103) Ziegler, J. F.; Biersack, J. P. *Treatise on heavy-ion science: volume 6: astrophysics, chemistry, and condensed matter*; Springer, 1985; pp 93–129.
- (104) aiida-qe-xspec: An AiiDA plugin designed for core-level spectroscopy calculations using Quantum ESPRESSO. <https://github.com/aiidaplugins/aiida-qe-xspec>, 2025.
- (105) Huber, S. P.; Zoupanos, S.; Uhrin, M.; Talirz, L.; Kahle, L. et al. AiiDA 1.0, a scalable computational infrastructure for automated reproducible workflows and data provenance. *Scientific Data* **2020**, *7*, 300.
- (106) Uhrin, M.; Huber, S. P.; Yu, J.; Marzari, N.; Pizzi, G. Workflows in AiiDA: Engineering a high-throughput, event-based engine for robust and modular computational workflows. *Computational Materials Science* **2021**, *187*, 110086.
- (107) Pedregosa, F.; Varoquaux, G.; Gramfort, A.; Michel, V.; Thirion, B. et al. Scikit-learn: Machine Learning in Python. *Journal of Machine Learning Research* **2011**, *12*, 2825–2830.
- (108) Chen, M. S.; Morawietz, T.; Mori, H.; Markland, T. E.; Artrith, N. AENET–LAMMPS and AENET–TINKER: Interfaces for accurate and efficient molecular dynamics simulations with machine learning potentials. *The Journal of Chemical Physics* **2021**, *155*, 074801.

- (109) Ferraresi, G.; Czornomaz, L.; Villevieille, C.; Novák, P.; El Kazzi, M. Elucidating the Surface Reactions of an Amorphous Si Thin Film as a Model Electrode for Li-Ion Batteries. *ACS Applied Materials & Interfaces* **2016**, *8*, 29791–29798.
- (110) Van der Marel, C.; Vinke, G.; Van der Lugt, W. The phase diagram of the system lithium-silicon. *Solid State Communications* **1985**, *54*, 917–919.
- (111) Aydinol, M. K.; Kohan, A. F.; Ceder, G.; Cho, K.; Joannopoulos, J. Ab initio study of lithium intercalation in metal oxides and metal dichalcogenides. *Phys. Rev. B* **1997**, *56*, 1354–1365.
- (112) Chevrier, V. L.; Dahn, J. R. First Principles Model of Amorphous Silicon Lithiation. *Journal of The Electrochemical Society* **2009**, *156*, A454.
- (113) Zhang, Q.; Cui, Y.; Wang, E. First-principles approaches to simulate lithiation in silicon electrodes. *Modelling and Simulation in Materials Science and Engineering* **2013**, *21*, 074001.
- (114) Iaboni, D. S. M.; Obrovac, M. N. Li<sub>15</sub>Si<sub>4</sub> Formation in Silicon Thin Film Negative Electrodes. *Journal of The Electrochemical Society* **2015**, *163*, A255.
- (115) Bärmann, P.; Krueger, B.; Casino, S.; Winter, M.; Placke, T. et al. Impact of the Crystalline Li<sub>15</sub>Si<sub>4</sub> Phase on the Self-Discharge Mechanism of Silicon Negative Electrodes in Organic Electrolytes. *ACS Applied Materials & Interfaces* **2020**, *12*, 55903–55912, PMID: 33259711.
- (116) Woodard, J. C.; Kalisvaart, W. P.; Sayed, S. Y.; Olsen, B. C.; Buriak, J. M. Beyond Thin Films: Clarifying the Impact of c-Li<sub>15</sub>Si<sub>4</sub> Formation in Thin Film, Nanoparticle, and Porous Si Electrodes. *ACS Applied Materials & Interfaces* **2021**, *13*, 38147–38160, PMID: 34362252.

- (117) Ref. 11 referenced the surface-hydrocarbon peak in the C 1s region, while Ref. 109 applied no energy calibration. This different calibration may result in systematic, inhomogeneous, and core-level-dependent energy offsets as previously observed in XPS measurements of cycled battery electrodes.<sup>?</sup> Additional discrepancies may also originate from the finite surface depth probed by XPS, which may result in an apparent Li content that differs from the local composition experienced by the photoelectrons.
- (118) Boniface, M.; Quazuguel, L.; Danet, J.; Guyomard, D.; Moreau, P. et al. Nanoscale Chemical Evolution of Silicon Negative Electrodes Characterized by Low-Loss STEM-EELS. *Nano Letters* **2016**, *16*, 7381–7388, PMID: 27960471.
- (119) Li, Y.; Zheng, X.; Cao, Z.; Wang, Y.; Wang, Y. et al. Unveiling the mechanisms into Li-trapping induced (ir)reversible capacity loss for silicon anode. *Energy Storage Materials* **2023**, *55*, 660–668.
- (120) Hernandez Bertran, M. A.; Zapata Dominguez, D.; Berhaut, C. L.; Tardif, S.; Longo, A. et al. Understanding the Irreversible Lithium Loss in Silicon Anodes Using Multi-edge X-ray Scattering Analysis. *Chemistry of Materials* **2025**, *37*, 3648–3660.
- (121) Kim, K. J.; Wortman, J.; Kim, S.-Y.; Qi, Y. Atomistic Simulation Derived Insight on the Irreversible Structural Changes of Si Electrode during Fast and Slow Delithiation. *Nano Letters* **2017**, *17*, 4330–4338, PMID: 28632390.

# SUPPORTING INFORMATION

## Tracking the Lithiation State of $\text{Li}_x\text{Si}$ from Machine-Learned XPS Binding Energies

Michael Alejandro Hernandez Bertran,<sup>†,‡</sup> Davide Tisi,<sup>¶</sup> Federico Grasselli,<sup>†,‡</sup>  
Michele Ceriotti,<sup>¶</sup> Elisa Molinari,<sup>†,‡</sup> and Deborah Prezzi<sup>\*,‡</sup>

<sup>†</sup>*Dipartimento di Scienze Fisiche, Informatiche, Matematiche (FIM), Università di  
Modena e Reggio Emilia, 41125 Modena, Italy*

<sup>‡</sup>*Nanoscience Institute, National Research Council (CNR-NANO), 41125 Modena, Italy*

<sup>¶</sup>*Laboratory of Computational Science and Modeling, Institut des Matériaux, École  
Polytechnique Fédérale de Lausanne, 1015 Lausanne, Switzerland*

E-mail: [deborah.prezzi@cnr.it](mailto:deborah.prezzi@cnr.it)

### Model hyperparameters and learning curves

Figure S1 shows the overall accuracy of the ML models for the predicted Li 1s (left) and Si 2p (right) BEs, relative to ab initio DFT for the validation set. This is represented by the MAE in eV, as a function of both the characteristic distances  $r_0$  used in the radial scaling of the SOAP descriptors and the number of local atomic environments in the training set. The effect of the different values of  $r_0$  on the MAE is visible when considering  $r_0=5.5$  Å and  $r_0=2.5$  Å, which produce the larger and smaller MAE values, respectively. Regardless of the value of  $r_0$ , the prediction error continues to decrease with the inclusion of additional environments in the training set, without reaching a saturation regime. The optimal SOAP

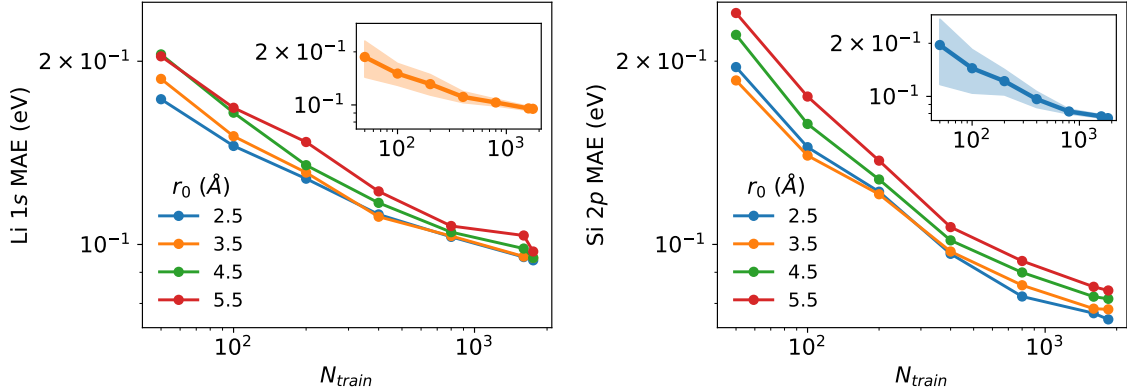


Figure S1: BE prediction error corresponding to the Li 1s (left) and Si 2p (right) models. The average MAE between the BEs predicted by the ML model and those obtained from DFT is shown on a log–log scale for different characteristic distances used in the radial scaling of the SOAP descriptor, as a function of the number of environments used for training  $N_{train}$ . For the selected characteristic distances an inset was added containing the average BE error (dot and line) with its uncertainty (shaded region) quantified as two times the standard deviation within the cross-validation folds.

and KRR Model parameters with the respective MAE and RMSE errors are reported in [Table S1](#).

Table S1: **Optimal SOAP and Model parameters reported with their respective MAE and RMSE errors.**

Core-level	SOAP		KRR		Errors (eV)	
	$r_0$ (Å)	$\sigma_a$ (Å)	$\lambda$	$\gamma$	MAE	RMSE
Li 1s	3.5	0.3	$2.98 \cdot 10^{-4}$	0.264	0.095	0.120
Si 2p	2.5	0.3	$6.95 \cdot 10^{-5}$	0.379	0.075	0.096

## Evaluation of the Li 1s and Si 2p models on the $\text{Li}_x\text{Si}$ dataset

In an amorphous solid, any observable  $A$  could be evaluated as a canonical ensemble average over a large number of thermodynamically accessible static configurations  $x_i$ . If  $A$  is defined as the binding energy value at which the XPS spectrum reaches its maximum intensity for

a given static configuration  $x_i$ , hereafter denoted  $\text{BE}_{max}^{x_i}$ , then its expected value over an amorphous  $\text{Li}_x\text{Si}$  phase can be written as

$$\text{BE}_{max}^x = \langle \text{BE}_{max}^{x_i} \rangle_i = \sum_{i=1}^N \frac{e^{-\beta\varepsilon(x_i)}}{Z_x} \text{BE}_{max}^{x_i}, \quad (1)$$

where  $N$  is the number of static configurations, or, in this case, structures, with the same Li concentration  $x$ ,  $\varepsilon(x_i)$  is the total energy per atom for the structure  $x_i$  and  $Z_x = \sum_{i=1}^N e^{-\beta\varepsilon(x_i)}$  is the partition function for the stoichiometry  $x$ .

Figure S2 shows  $\text{BE}_{max}^x$  for the Li 1s (top) and Si  $2p^{3/2}$  (bottom) XPS spectrum as a function of the Li concentration. The blue squares represent the values calculated using the ML predictions over the full  $\text{Li}_x\text{Si}$  dataset<sup>1</sup> split in crystalline (left) and amorphous (right) structures, while the orange stars correspond to the values obtained from DFT calculations on the training set. The standard deviation for a given stoichiometry present in the dataset is represented by the blue area. For the Li 1s spectrum, no clear trend of  $\text{BE}_{max}^x$  with respect to Li concentration is detected, neither for crystalline nor amorphous structures. In contrast, for the Si  $2p^{3/2}$  spectrum, a clear downward trend of  $\text{BE}_{max}^x$  is observed in both structural types, with marked jumps in the crystalline dataset within the  $1 < x < 2$  region. For the  $\text{Li}_x\text{Si}$  dataset, the  $\text{BE}_{max}^x$  predicted by the model shows a smooth variation (except around  $x \approx 2$ ) with a small error in the  $0 < x < 1.5$  region. This trend is less apparent when using only the ab initio results from the training set, suggesting that convergence has not yet been achieved with respect to the number of static configurations used.

## Energetics and parameters convergence in grand canonical Monte Carlo simulations

Convergence tests were carried out on the BE values computed along the GCMC trajectories by reducing the acceptance ratio (from 44 to 27%, see Figure S3, left panel), and increasing

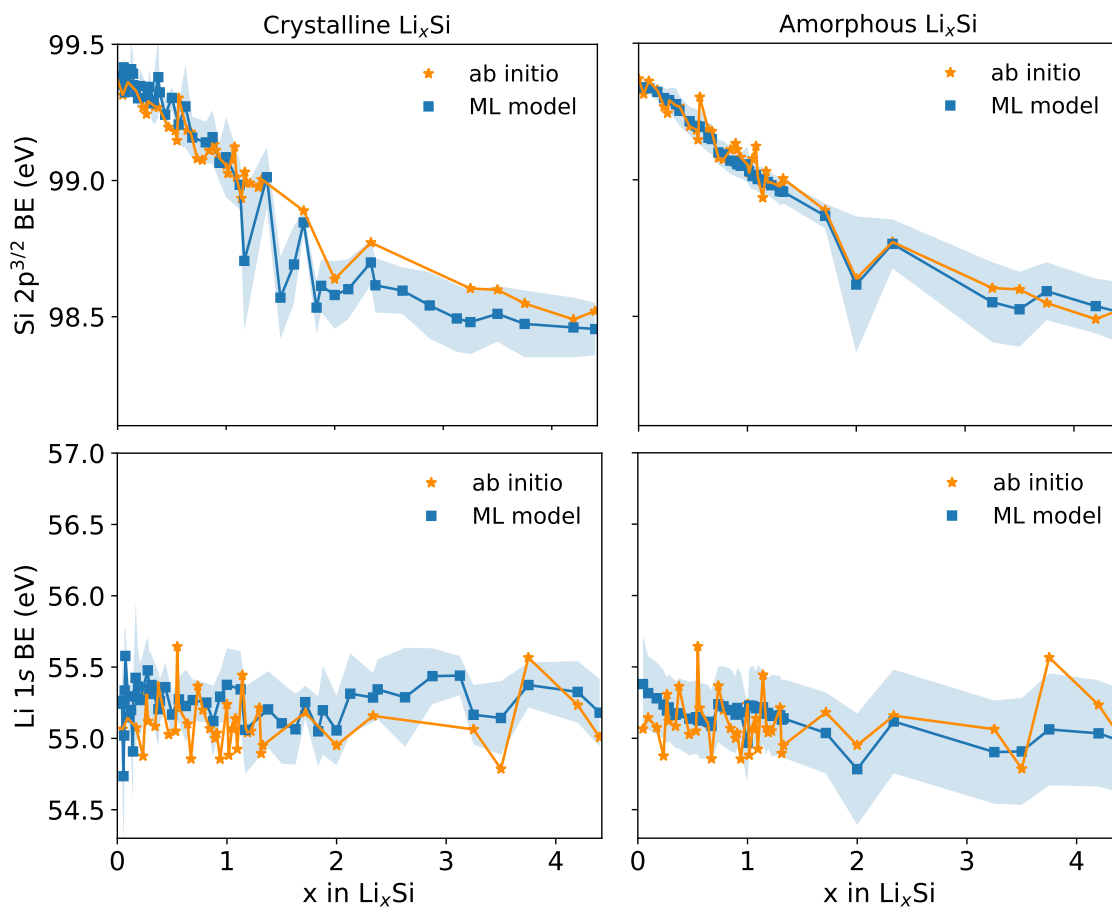


Figure S2: Stoichiometry maps showing the average peak position of Li 1s (top) and Si 2p<sup>3/2</sup> (bottom) for the c-Li<sub>x</sub>Si (left) and a-Li<sub>x</sub>Si (right) structures in the Li<sub>x</sub>Si dataset. Blue squares represent ML model predictions, while orange stars denote ab initio calculations performed on the training set. The shaded blue region represents the standard deviation of the BEs for each stoichiometry.

the number of MD steps per MC move (from 50 to 100, see Figure S3, central panel). No significant changes were observed in the predicted BE values, confirming the robustness of the results with respect to the MC sampling. We observe instead a dependence on the system size (see Figure S3, right panel), and in particular, on the number of Si atoms required to obtain converged results in the region of low Li concentration. Importantly, convergence was only achieved for systems containing 8000 Si atoms (within an initial  $\text{Li}_{3.75}\text{Si}$  cell of 76000 atoms).

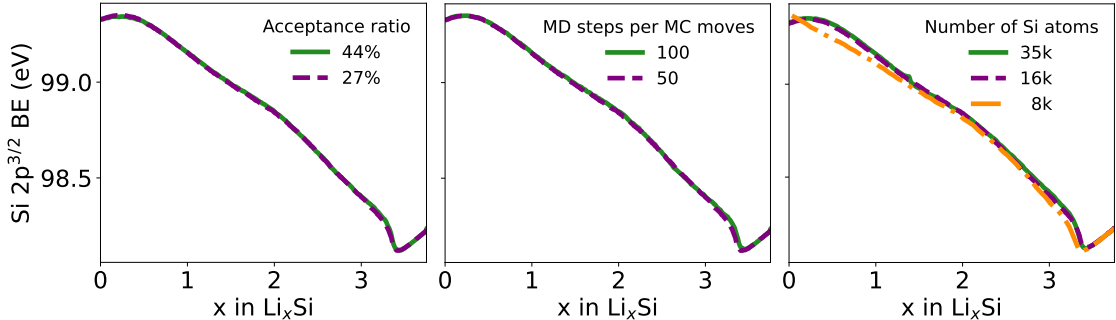


Figure S3: Convergence tests for the acceptance ratio (left), MD steps (center), and system size (right) performed for the GCMC simulation initiated from  $\text{c-Li}_{3.75}\text{Si}$

## XPS Data Processing and Alignment Details

Experimental *ex situ* and *operando* XPS data were extracted from Ref. 2 and Ref. 3, respectively, using the PlotDigitizer software.<sup>4</sup> For a-Si thin films (30 nm in Ref. 2 and 95 nm in Ref. 3), Li diffusion is known to be sufficiently fast ( $D_{\text{Li}} \approx 10^{-14} - 10^{-12} \text{cm}^2/\text{s}$ )<sup>5-9</sup> to ensure nearly uniform Li distribution across the film thickness over the galvanostatic cycling times reported in these studies ( $\approx 1$  h and  $\approx 15$  h for (de)lithiation, respectively). Under this hypothesis, we can consider the electrode potential as a reliable proxy for the approximated average Li content in the thin-film a-Si. Accordingly, the  $\text{BE}_{\text{max}}-V$  data in Ref. 2 were mapped onto  $\text{BE}_{\text{max}}-x$  using the corresponding lithiation state as a function of potential reported in Ref. 3. In addition, it is worth noting that Ref. 3 referenced all spectra to the

surface-hydrocarbon peak (C 1s region), while the spectra in Ref. 2 were provided without calibration. To enable a consistent comparison between the two experimental datasets and with our calculated BEs on a common reference scale, the  $BE_{max}$  values from Ref. 3 were rigidly shifted to align their energy scale with that of Ref. 2 in the low-lithiation region. The different applied shifts ( $\Delta E = 2.86$  eV for Li 1s and  $\Delta E = 1.8$  eV for Si 2p) reflect the fact that differential charging can lead to non-uniform offsets between core levels associated with distinct chemical environments.<sup>10-14</sup> Finally, since the Li 1s  $BE_{max}$  value corresponding to  $Li_xSi$  was not explicitly reported in Ref. 2, the Li 1s spectrum was refitted in this work to isolate the contribution associated with the  $Li_xSi$  phase, as illustrated in Figure S4.

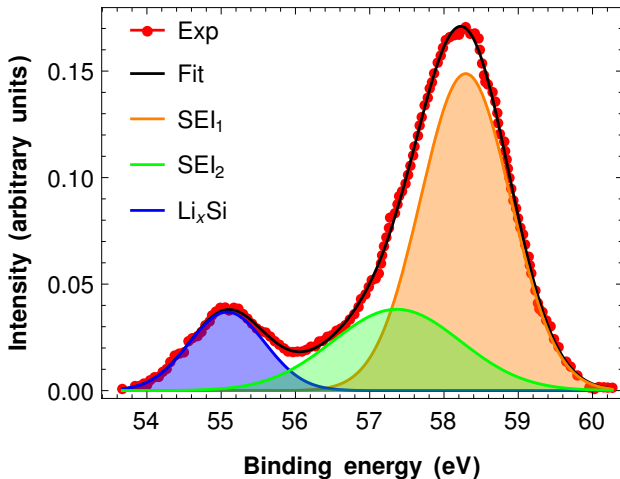


Figure S4: Example of the Li 1s curve-fitting result for Si electrode data at 0.07 V during delithiation, extracted from Ref. 2 (red points). The fitted components correspond to the various SEI species and the  $Li_xSi$  contribution.

## Formation energy and convex hull from GCMC simulations

Figure S5 presents the formation energy per Si atom and the corresponding convex hull obtained from GCMC simulations starting at different Li concentrations. The convex hull represents the formation energy as a function of composition, where the envelope connects

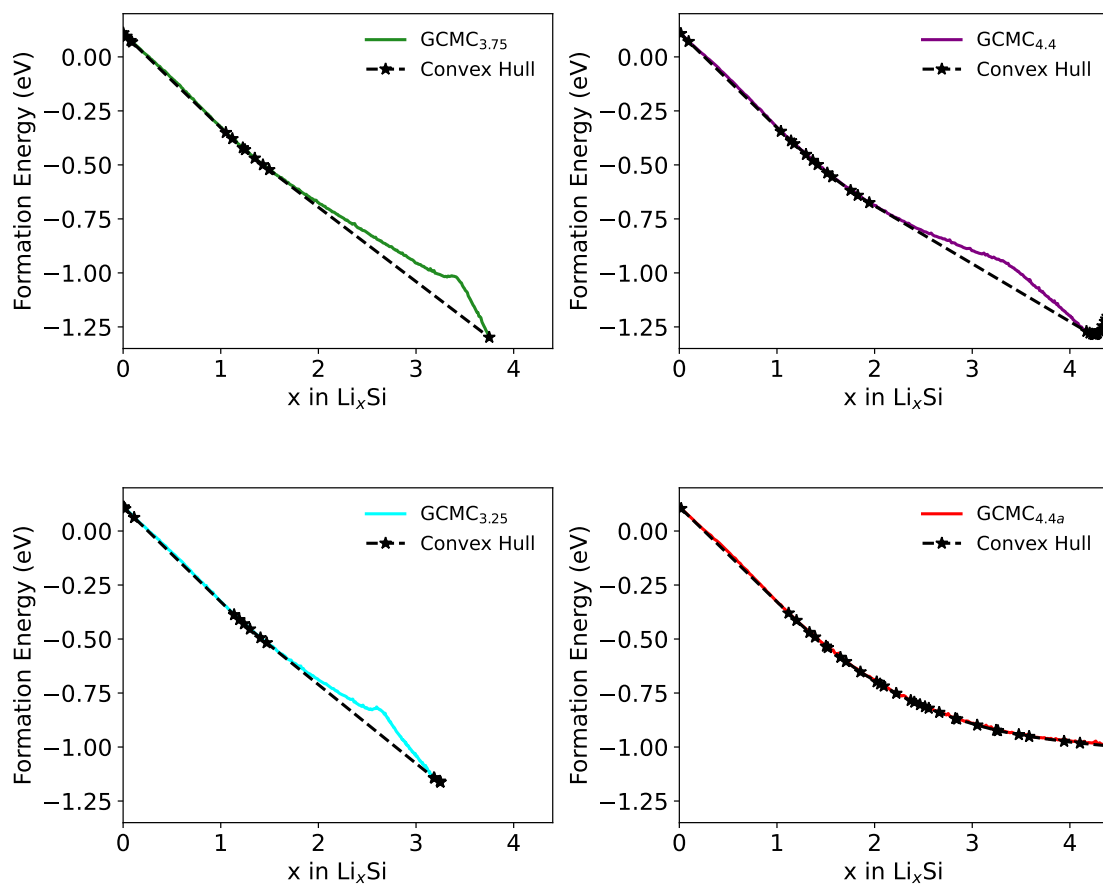


Figure S5: Formation energy per Si atom and convex hull from GCMC simulations starting from  $c\text{-Li}_{3.75}\text{Si}$  (green),  $c\text{-Li}_{4.4}\text{Si}$  (purple),  $a\text{-Li}_{4.4}\text{Si}$  (red) and  $c\text{-Li}_{3.25}\text{Si}$  (cyan).

the thermodynamically stable phases, bounding metastable and unstable phases above it. Furthermore, the slope of each line segment connecting adjacent points on the convex hull corresponds to the associated voltage value between the two phases.

Figure S6 shows the stoichiometry dependence of the Si  $2p^{3/2}$  FWHM. In the low-Li concentration regime, the FWHM values obtained from the MQA (red solid line) and GCMC (green solid line) structures are in good agreement with each other and with *operando* experimental data<sup>3</sup> (black crosses). At  $x \approx 3.4$ , however, the experimental FWHM exhibits a characteristic peak associated with the amorphization of the c-Li<sub>3.75</sub>Si phase formed during lithiation. This feature is qualitatively reproduced only by the GCMC-generated structures, although shifted at higher concentrations, supporting the attribution to the crystal-to-amorphous transition.

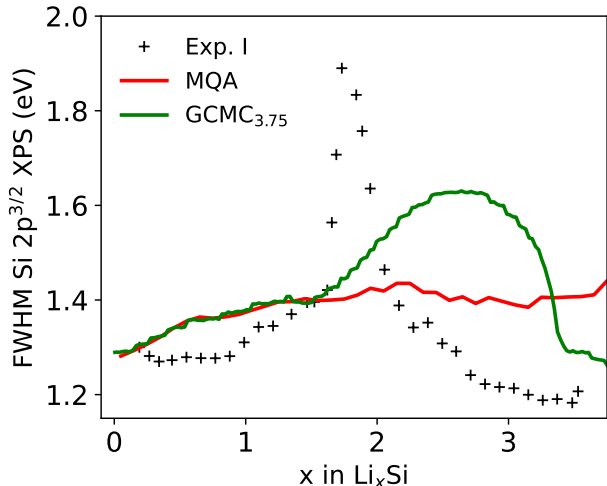


Figure S6: FWHM of Si  $2p^{3/2}$  for  $\text{Li}_x\text{Si}$  structures generated using MQA (red) and GCMC departing from c-Li<sub>3.75</sub>Si (green), compared to experimental data for Si electrodes from Ref. 3 (black crosses).

## References

- (1) Fu, F.; Wang, X.; Zhang, L.; Yang, Y.; Chen, J. et al. Unraveling the Atomic-scale Mechanism of Phase Transformations and Structural Evolutions during (de)Lithiation

- in Si Anodes. *Advanced Functional Materials* **2023**, *33*, 2303936.
- (2) Ferraresi, G.; Czornomaz, L.; Villevieille, C.; Novák, P.; El Kazzi, M. Elucidating the Surface Reactions of an Amorphous Si Thin Film as a Model Electrode for Li-Ion Batteries. *ACS Applied Materials & Interfaces* **2016**, *8*, 29791–29798.
- (3) Endo, R.; Ohnishi, T.; Takada, K.; Masuda, T. Electrochemical Lithiation and Delithiation in Amorphous Si Thin Film Electrodes Studied by Operando X-ray Photoelectron Spectroscopy. *The Journal of Physical Chemistry Letters* **2022**, *13*, 7363–7370.
- (4) PlotDigitizer: Version 3.1.6. 2025; <https://plotdigitizer.com>.
- (5) Hatchard, T. D.; Dahn, J. R. In Situ XRD and Electrochemical Study of the Reaction of Lithium with Amorphous Silicon. *Journal of The Electrochemical Society* **2004**, *151*, A838.
- (6) Kulova, T.; Skundin, A.; Pleskov, Y.; Terukov, E.; Kon'kov, O. Lithium insertion into amorphous silicon thin-film electrodes. *Journal of Electroanalytical Chemistry* **2007**, *600*, 217–225, Equilibrium and kinetics of electrode processes.
- (7) Ding, N.; Xu, J.; Yao, Y.; Wegner, G.; Fang, X. et al. Determination of the diffusion coefficient of lithium ions in nano-Si. *Solid State Ionics* **2009**, *180*, 222–225.
- (8) Xie, J.; Imanishi, N.; Zhang, T.; Hirano, A.; Takeda, Y. et al. Li-ion diffusion in amorphous Si films prepared by RF magnetron sputtering: A comparison of using liquid and polymer electrolytes. *Materials Chemistry and Physics* **2010**, *120*, 421–425.
- (9) Wang, J. W.; He, Y.; Fan, F.; Liu, X. H.; Xia, S. et al. Two-Phase Electrochemical Lithiation in Amorphous Silicon. *Nano Letters* **2013**, *13*, 709–715, PMID: 23323743.
- (10) Metson, J. Charge compensation and binding energy referencing in XPS analysis. *Surface and Interface Analysis: An International Journal devoted to the development and*

*application of techniques for the analysis of surfaces, interfaces and thin films* **1999**, *27*, 1069–1072.

- (11) Oswald, S. Binding energy referencing for XPS in alkali metal-based battery materials research (I): Basic model investigations. *Applied Surface Science* **2015**, *351*, 492–503.
- (12) Baer, D. R.; Engelhard, M. H.; Gaspar, D. J.; Lea, A. S.; Windisch Jr, C. Use and limitations of electron flood gun control of surface potential during XPS: two non-homogeneous sample types. *Surface and Interface Analysis: An International Journal devoted to the development and application of techniques for the analysis of surfaces, interfaces and thin films* **2002**, *33*, 781–790.
- (13) Suzer, S. Differential Charging in X-ray Photoelectron Spectroscopy: A Nuisance or a Useful Tool? *Analytical Chemistry* **2003**, *75*, 7026–7029, PMID: 14670067.
- (14) Dubey, M.; Raman, A.; Gawalt, E. S.; Bernasek, S. L. Differential charging in X-ray photoelectron spectroscopy for characterizing organic thin films. *Journal of Electron Spectroscopy and Related Phenomena* **2010**, *176*, 18–23, Charging Issues in Electron Spectroscopies.

# TOC Graphic

